Article

CO$_2$ Methanation over Nickel Catalysts: Support Effects Investigated through Specific Activity and Operando IR Spectroscopy Measurements

Vigni V. González-Rangulan [1], Inés Reyero [1], Fernando Bimbela [1], Francisca Romero-Sarria [2], Marco Daturi [3] and Luis M. Gandía [1,*]

1. Grupo de Reactores Químicos y Procesos para la Valorización de Recursos Renovables (QuiProVal), Institute for Advanced Materials and Mathematics (InaMat2), Departamento de Ciencias, Universidad Pública de Navarra (UPNA), 31006 Pamplona, Spain
2. Departamento de Química Inorgánica, Instituto de Ciencia de Materiales de Sevilla, Centro Mixto Universidad de Sevilla-CSIC, Avda. Américo Vespucio 49, 41092 Sevilla, Spain
3. Laboratoire Catalyse et Spectrochimie, CNRS, UNICAEN, ENSICAEN, Normandie Université, 14050 Caen, France
* Correspondence: lgandia@unavarra.es

Abstract: Renewed interest in CO$_2$ methanation is due to its role within the framework of the Power-to-Methane processes. While the use of nickel-based catalysts for CO$_2$ methanation is well stablished, the support is being subjected to thorough research due to its complex effects. The objective of this work was the study of the influence of the support with a series of catalysts supported on alumina, ceria, ceria–zirconia, and titania. Catalysts' performance has been kinetically and spectroscopically evaluated over a wide range of temperatures (150–500 °C). The main results have shown remarkable differences among the catalysts as concerns Ni dispersion, metallic precursor reducibility, basic properties, and catalytic activity. Operando infrared spectroscopy measurements have evidenced the presence of almost the same type of adsorbed species during the course of the reaction, but with different relative intensities. The results indicate that using as support of Ni a reducible metal oxide that is capable of developing the basicity associated with medium-strength basic sites and a suitable balance between metallic sites and centers linked to the support leads to high CO$_2$ methanation activity. In addition, the results obtained by operando FTIR spectroscopy suggest that CO$_2$ methanation follows the formate pathway over the catalysts under consideration.

Keywords: carbon dioxide; hydrogenation; methane; nickel catalysts; operando FTIR; support; TOF

1. Introduction

The methanation of carbon oxides is an important and well-stablished process in ammonia and hydrogen synthesis plants. After natural-gas steam reforming, water–gas shift stages, and CO$_2$ removal, CO and CO$_2$ are still present at combined concentrations typically below 1 vol.% in a hydrogen-rich stream. These carbon oxides are almost quantitatively converted into CH$_4$ over nickel catalysts in two methanators, connected in series, at reaction temperatures between about 300 and 450 °C [1]. Historically, the production of substitute natural gas (SNG) through the methanation of the gases obtained from some oil products or coal has also been important. This process was developed in times (late 1960s to the 1980s) when there was a fear surrounding the availability of natural gas [1,2]. In this case, the steam gasification of naphtha, liquefied petroleum gas (LPG), coal, and, more recently, biomass, leads to streams containing CH$_4$, H$_2$, H$_2$O, and carbon oxides at concentrations (0.5–31 vol. % CO and 10–25 vol.% CO$_2$) that depend on the feedstock and gasification conditions. The methanation of these streams over nickel catalysts, conducted in one or two stages with partial recycling of the product to limit the temperature rise, allows us to increase their heating values to suitably high rates [1–6].

Renewed interest in methanation has arisen mainly due to its role within the framework of the Power-to-X processes, also denoted as P2X or PtX, by which hydrogen obtained through water electrolysis coupled to renewable electricity sources is used to produce chemicals and fuels with reduced carbon footprints [7,8]. PtX is an "umbrella" term, where X can stand for hydrogen, syngas, methane, methanol, ammonia, olefins, synthetic fuels, etc. As for Power-to-Methane (PtM) processes, methanation and water electrolysis are the key steps [9–13]. The most obvious application of the produced methane is its injection in the low-pressure natural gas grid, though other uses, such as in transportation as compressed natural gas (CNG) and industrial processes, are also envisaged. The carbon source (CO and CO_2) is, of course, of great importance. Ideally, it should be of biogenic origin to enable users to achieve very low carbon footprints of the produced methane [14] and should contain carbon oxides in high concentration to avoid efficiency losses and costs associated with carbon capture. In this regard, biogas is perhaps the most relevant carbon source [9,10,15]. It can be subjected to methanation after suitable purification to remove compounds that can deactivate the catalysts or jeopardize the quality of the final product. Alternatively, CO_2 can be obtained as a concentrated stream from the biogas-upgrading plants that produce biomethane. Another option is to hydrogenate the carbon oxides obtained after biomass gasification; in this case, the product gas fed to the methanator also contains CH_4 and H_2. The combination of water electrolysis and biomass gasification is a very appealing process because the electrolytic oxygen can be used in the gasifier, whereas the hydrogen is used to increase the H/C ratio of the methanator feed stream to suitable values [15,16]. In this way, it is possible to greatly increase the production of methane compared with the methanation of the product gas obtained after steam gasification once subjected to a water–gas shift step.

Methanation reactions imply large changes of the oxidation state of the carbon atom; therefore, they are characterized by strong kinetic barriers. As a result, active catalysts are necessary to carry out methanation at reasonably low temperatures as those required to overcome the thermodynamic limitations also existing due to the reversible exothermic character of the reaction. Typical methanation catalysts are made of nickel supported on γ-Al_2O_3 or SiO_2 and frequently contain low amounts of MgO [1,17]. These catalysts have been widely investigated [18,19], and recent research in this field has led to a plethora of scientific literature discussing their ongoing development [20–31]. Nickel has been traditionally the active phase of choice since, after careful catalyst formulation and preparation, it presents a good balance between its performance in terms of activity, selectivity, and lifetime and its cost. Generally, nickel is present in the catalyst precursor as oxide at high loads. The precursor has to be easily reducible to the active metallic state at temperatures (typically about 300 °C) at which the feed stream enters the reactor, though it can be loaded pre-reduced (and passivated) into the methanator. The use of promoters such as alkali and alkaline earth metals and lanthanides [29], as well as bimetallic Ni-M (M = Fe, Co, Cu, Ru, Rh, Pt, Pd, and Re) [30] formulations have been frequently considered in order to improve the activity and stability of nickel-based CO_2 methanation catalysts. The support also plays a very important role in the performance of the methanation catalyst, providing a porous matrix on which Ni can be finely divided in the form of nanometer-size crystallites, thus achieving a good dispersion of the active phase, while avoiding, or at least retarding, sintering. This is a key aspect given the high exothermicity of the CO_2 methanation reaction ($\Delta H_{573K}^{0} = -177.6$ kJ/mol) that increases the risk of hot spots formation in the fixed-bed reactors that are normally used. Therefore, selecting the support (and catalyst preparation method) is a compromise between opposite requirements: on the one hand, easy reducibility of the nickel species is essential, whereas achieving a sufficient degree of interaction with the support is indispensable to guarantee suitable metallic dispersion under working conditions [1]. In addition to these structural effects [32–36], recent studies have revealed that the support can also participate in the catalytic cycle, affecting CO_2 adsorption and activation, as well as the methanation reaction pathways [22,37].

The nature and strength of the basic sites of the supports are frequently considered to be responsible for the formation and subsequent evolution of the CO_2 methanation

intermediates, thus greatly affecting the catalyst activity and selectivity [38–44]. In addition, a key role is also attributed to the interfacial region between the support and the metallic particles of the reduced catalyst [45–48]. In the case of certain metal oxides acting as supports of methanation catalysts, that region is considered to have a polyfunctional character and is believed to accommodate active sites capable of activating CO_2, which is further hydrogenated thanks to the close presence of hydrogen atoms on the surface of the metallic particles. Furthermore, electronic effects and strong metal–support interaction phenomena associated with the metal/support interface have also been claimed as features that affect the performance of some CO_2 methanation catalysts.

The ensemble of the vast experimental works performed so far in the search for catalyst properties–performance relationships, together with the use of advanced characterization techniques, most notably operando IR spectroscopy [49,50], and theoretical studies have allowed researchers to make big advances in the understanding of the mechanism and the structure sensitivity character of the methanation of CO_2 over nickel catalysts [45,51–56]. However, its mechanism is still debated, and catalysts that are more efficient are searched for industrial applications in view of the necessity to capture and reuse carbon dioxide, as well as to handle the present shortage of natural gas in many regions of the world. Therefore, additional studies on this topic are necessary because there are important aspects, such as some structural requirements of the catalyst, the sequence of elementary steps, or the nature of the reaction intermediates leading to CH_4 or CO, that remain controversial [57].

The main aim of the present work was to assess the performance in the CO_2 methanation reaction of nickel catalysts supported on alumina, ceria, a ceria–zirconia mixed oxide, and titania. This set of supports includes both reducible and irreducible metal oxides, and it opens the door to the establishment of different types of metal–support interactions that are expected to lead to different activities and selectivities. It is hoped that this way would provide information that contributes to a rational design of methanation catalysts based on nickel. Catalysts' performance has been evaluated through catalytic tests conducted over a very wide range of reaction temperatures (150–500 °C), as well as through specific activity (turnover frequency (TOF) and apparent activation energies) and operando infrared spectroscopy (FTIR) measurements.

2. Results

2.1. Physicochemical Characterization of the Catalysts

A selection of the physicochemical properties of the nickel catalysts investigated in the present work is offered in Table 1. The actual Ni contents ranged between 7.6 and 8.9 wt.%, and they were reasonably close to the nominal content (10 wt.%). The specific surface area (S_{BET}) values of the catalysts were between 9% and 20% lower than those of the supports (see Section 4.1). The highest value corresponded to the Ni catalyst supported on γ-Al_2O_3 (Ni/Al), and the lowest corresponded to the titania-supported one (Ni/Ti), whereas the catalysts supported on ZrO_2-CeO_2 (Ni/ZrCe) and ceria (Ni/Ce) exhibited similar intermediate S_{BET} values.

Table 1. Physicochemical properties of the supported nickel catalysts.

Catalyst	Ni Content (wt.%)	S_{BET} (m^2/$g_{cat.}$)	Metallic Ni Surface Area (S_{Ni}, m^2/g_{Ni})	Degree of Reduction (DOR_{Ni}, %)	Nickel Dispersion (D_{Ni}, %)	Mean Ni Particle Size (d_{Ni}, nm)
Ni/Al	7.6	201	41.7	68.9	6.3	7.1
Ni/Ce	8.2	93	34.3	103	5.1	13
Ni/ZrCe	8.9	87	19.1	131	2.9	23
Ni/Ti	8.7	53	8.1	120	1.2	67

As for the metallic surface area and dispersion, substantial differences were found among the catalysts, with Ni/Al and Ni/Ti again being the samples showing the highest

and lowest values, respectively. Ni/Ce exhibited relatively high metallic Ni surface area and dispersion, though lower than the values of Ni/Al, whereas Ni/ZrCe showed intermediate values of those structural parameters. As a result, the mean Ni particle size of the catalysts followed the increasing order of Ni/Al < Ni/Ce < Ni/ZrCe < Ni/Ti, with values ranging from 7.1 to 67 nm. It should be highlighted that only Ni/Al showed an incomplete degree of reduction of nickel (DOR$_{Ni}$) after the H$_2$ reduction activation procedure employed before the chemisorption and catalytic performance assessment experiments. Values of DOR$_{Ni}$ slightly above 100% were obtained for Ni/Ce, whereas DOR$_{Ni}$ reached up to 120% and 131% for Ni/Ti and Ni/ZrCe. In these cases, it has been assumed that the reduction of Ni is complete and that the extra consumption of oxygen is due to the reoxidation of the partially reduced supports. It is well-known that these supports are reducible and that their reducibility increases after depositing metals on them such as Ni, which is capable of activating H$_2$ and provoking hydrogen spillover during catalysts activation. Oxygen vacancies created during the activation of the catalysts supported on reducible oxides can be refilled by O$_2$ during the measurement of DOR$_{Ni}$, leading to values above 100 % in such cases.

The X-ray diffraction (XRD) patterns of the catalysts obtained after calcination are shown in Figure 1. In addition to NiO, all the supported catalysts presented the crystalline phases expected for each support: γ-alumina for Ni/Al, fluorite-structured CeO$_2$ for Ni/Ce, and rutile and anatase for Ni/Ti. In the case of the Ni/ZrCe catalyst, (Zr$_{0.88}$Ce$_{0.12}$)O$_2$ was identified as the main crystalline phase, though the presence of ZrO$_2$ (baddeleyite) in small amounts cannot be ruled out. NiO peaks are broad in the XRD pattern of Ni/Al, indicating a relatively good dispersion of Ni on γ-alumina. The rest of the supports are highly crystalline, as evidenced by the high intensity of the corresponding XRD peaks. Even so, weak NiO XRD peaks can also be appreciated, and this is possible due to the poor dispersion achieved on ZrO$_2$-CeO$_2$, and especially titania, that leads to big NiO crystallites.
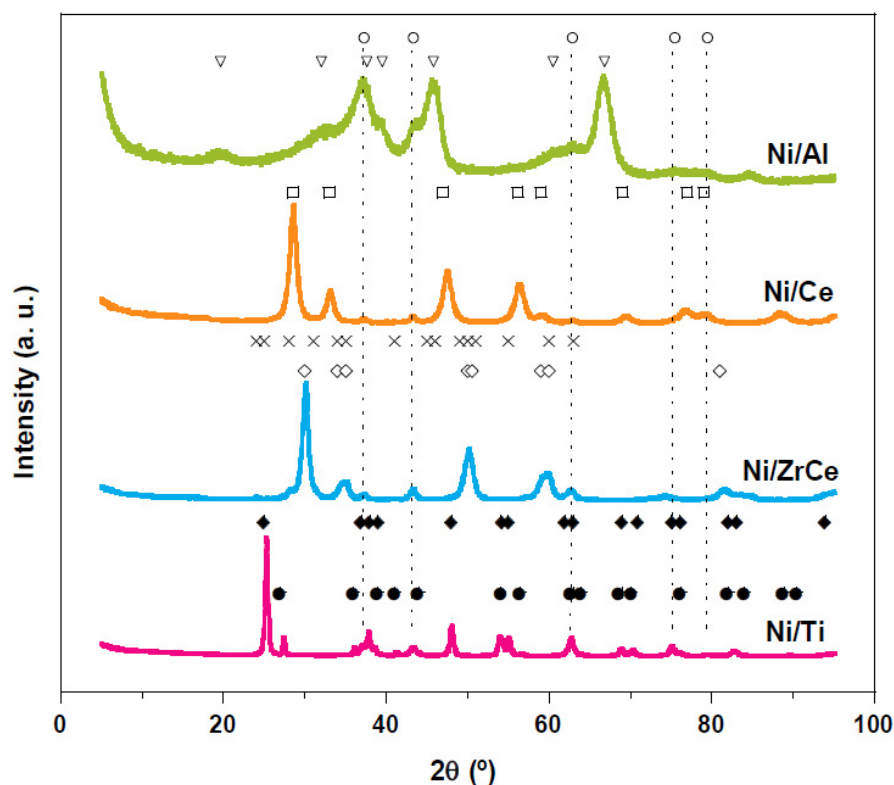

Figure 1. XRD patterns of the calcined supported Ni catalysts. Crystalline phases identified: (○) NiO, (▽) γ-Al$_2$O$_3$, (□) CeO$_2$, (◇) (Zr$_{0.88}$Ce$_{0.12}$)O$_2$, (×) ZrO$_2$ baddeleyite, (◆) TiO$_2$ anatase, and (●) TiO$_2$ rutile.

The H_2-TPR profiles of the calcined supported nickel catalysts are presented in Figure 2. As for the Ni/Al catalyst, the profile includes two contributions, in accordance with the findings from Bentaleb and Marceau [58]. The first one appears as a broad peak centered at 540 °C that can be attributed to the reduction of well-dispersed nickel oxide species strongly interacting with the support. A second reduction event that appears at a much higher temperature (753 °C) is ascribed to the presence of surface nickel aluminate, which is much more difficult to reduce. It is well-known that Ni^{2+} ions can diffuse occupying some of the octahedral and tetrahedral vacancies of the γ-Al_2O_3 structure, thus allowing the formation of stable $NiAl_2O_4$ surface spinels through solid-state reaction during catalyst calcination [58–60]. The presence of surface spinels would explain the incomplete degree of reduction achieved upon catalyst activation, with a value of about 70%, which is typical of this type of catalyst [58]. In addition, the presence of spinels evidences an interaction between the Ni precursors and the alumina support that can contribute to the higher dispersion of Ni in Ni/Al compared to the other catalysts (see Table 1). It should be noted that these spinels are typically hardly detectable by XRD due to their surface nature, and then, poorly ordered character, as well as to their low concentration, linked to the also low nickel content of the catalyst. In addition, there is much overlapping between the diffraction peaks of alumina and nickel aluminate due to their very close crystalline structure.
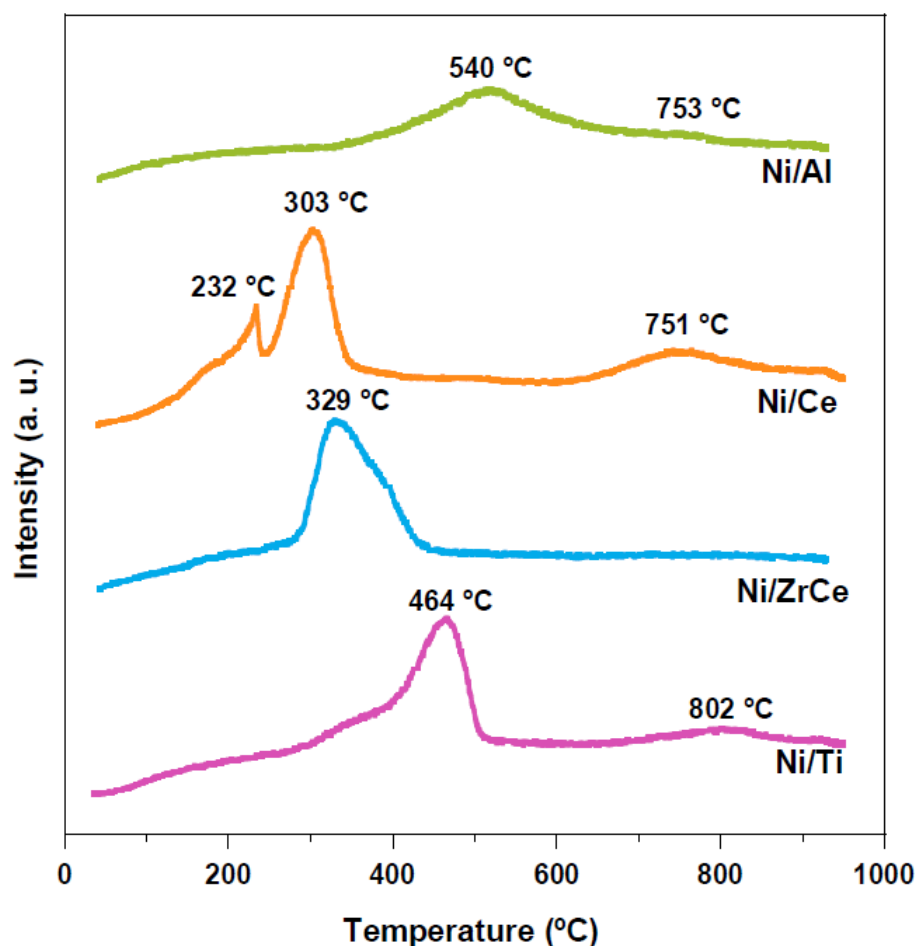

Figure 2. H_2-TPR profiles of the calcined supported nickel catalysts.

In the case of the Ni/Ce catalyst, the H_2-TPR profile presents three distinctive reduction events with maxima at 232, 303, and 751 °C, respectively. In addition, a weak and broad reduction peak can be appreciated at temperatures below 200 °C. The low-temperature (below 250 °C) events can be ascribed to the reduction of oxygen species adsorbed on oxygen vacancies associated with surface $Ni_xCe_{1-x}O_{2-\delta}$ solid solution formed during

catalyst preparation through partial replacement of Ce^{4+} cations by Ni^{2+} [61–65]. The reduction of very well dispersed NiO species has also been considered to take place between 220 and 240 °C [62–64]. These reduction events evidence the establishment of a strong interaction between Ni and CeO_2 [61]. The intense reduction peak at 303 °C includes most of the reducible species and is ascribed to large NiO particles supported over ceria [62–64]. This reduction event shifts toward higher temperatures as the catalyst nickel content increases [66]. Lastly, the weak and broad peak recorded at 751 °C is associated with the partial reduction of Ce^{4+} cations in bulk CeO_2. The temperature at which this peak appears depends on the textural properties of the support; it typically decreases as the specific surface area increases [67]. As for the Ni/ZrCe catalyst, a reduction event appears in the H_2-TPR profile that seems to be the result of at least two main contributions corresponding to peaks with maxima at around 330 and 400 °C, respectively. According to the study by Ocampo et al. [68] with a series of Ni catalyst supported on $Ce_{0.72}Zr_{0.28}O_2$, the first, more intense peak can be ascribed to the reduction of bulk NiO having a weak interaction with the support. Moreover, the second contribution could be due to the reduction of Ni^{2+} incorporated into the fluorite structure and in strong interaction with the mixed oxide. A similar interpretation has been given by Vrijburg et al. [69], who attributed an intense reduction event around 350 °C to the reduction of bulk NiO, and a second peak at 400 °C to the reduction of Ni^{2+} in strong interaction with the support that, in this case, was $Ce_{0.5}Zr_{0.5}O_2$. The H_2-TPR results show that Ni has established a stronger interaction with the support in Ni/Ce than in Ni/ZrCe, perhaps due to the low cerium content of the mixed oxide used. That interaction could explain the better dispersion achieved by Ni in Ni/Ce in spite of the close specific surface areas of the supports (see Table 1).

As concerns the Ni/Ti catalyst, two distinct reduction events can be distinguished in the TPR profile. The main reduction event is complex and characterized by a steady increase of the H_2 consumption in the 300–400 °C interval, then peaking at 464 °C and ending at around 500 °C. The second reduction event is much less intense, consisting in a broad peak with a maximum at 802 °C. The H_2-TPR profile of the Ni/Ti catalyst is rather similar to the ones recorded by Unwiset et al. [70] with a series of 3–20 wt.% Ni/TiO_2 catalysts prepared by a sol–gel procedure from Ni and Ti precursors. The continuous H_2 consumption starting at about 250 °C and peaking at 400–440 °C, depending on the Ni content, was attributed to the reduction of Ni^{2+} exhibiting interactions of different intensity with the support. According to van de Loosdrecht et al. [71], reduction events between 260 and 480 °C correspond first to the reduction of NiO and also to the reduction of nickel titanate ($NiTiO_3$) at temperatures above 330 °C. Ho et al. [72] calculated that only 47% of Ni is present as NiO in a 6 wt.% Ni/TiO_2 catalyst calcined at 500 °C, though $NiTiO_3$ could be detected through X-ray diffraction measurements in the sample calcined at 600 °C. In our case, nickel titanate is not present in the XRD pattern of the Ni/Ti catalyst (Figure 1), which was calcined at 500 °C, but, according to the mentioned literature, the H_2-TPR results suggest that it may be present in a surface amorphous and/or well-dispersed state. Finally, the broad peak centered at about 800 °C can be ascribed to the partial reduction of Ti^{4+} to Ti^{3+} in bulk TiO_2.

The CO_2-TPD profiles of the supported nickel catalysts recorded after hydrogen reduction for 3 h at 500 °C are shown in Figure 3. Total amounts of CO_2 desorbed (in μmol per g of catalyst) follow the order of Ni/Al (386) > Ni/ZrCe (347) > Ni/Ce (196) > Ni/Ti (71). Clearly, there are remarkable qualitative and quantitative differences between the results obtained with these catalysts.

According to Pan et al. [39], three types of basic sites can be distinguished depending on the CO_2 desorption temperature: weak (<250 °C), medium (between 250 and 700 °C), and strong (>700 °C). Based on this classification, all the catalysts considered in the present study have weak basic sites, which are particularly abundant in the case of Ni/Al. Moreover, Ni/Zr-Ce and Ni/Ti catalysts mainly exhibit weak basic sites. Medium-strength basic sites predominate in Ni/Ce and, to a lesser extent, in Ni/Al. Lastly, only Ni/Ce exhibits a significant amount of strong basic sites. Of course, this categorization is somewhat

arbitrary. Indeed, Liang et al. [42] ascribed to physical adsorption or adsorption on weak basic sites the CO_2 desorbed within 100–200 °C. In addition, desorption between 200 and 400 °C corresponded to medium-strength sites, whereas, between 500 and 600 °C, it was attributed to the strongest basic sites. The interpretation of our results does not change substantially by applying any of these criteria. According to Italiano et al., low-temperature CO_2 desorption corresponds to weakly bonded bicarbonate species formed upon CO_2 adsorption on surface hydroxyls (OH^-). On the other hand, bidentate carbonates from medium-strength sites consisting in metal-O^{2-} pairs, and monodentate carbonates from strong basic sites consisting in coordinatively unsaturated O^{2-} ions, are related to the desorption events taking place at medium and high temperatures, respectively [37,66].
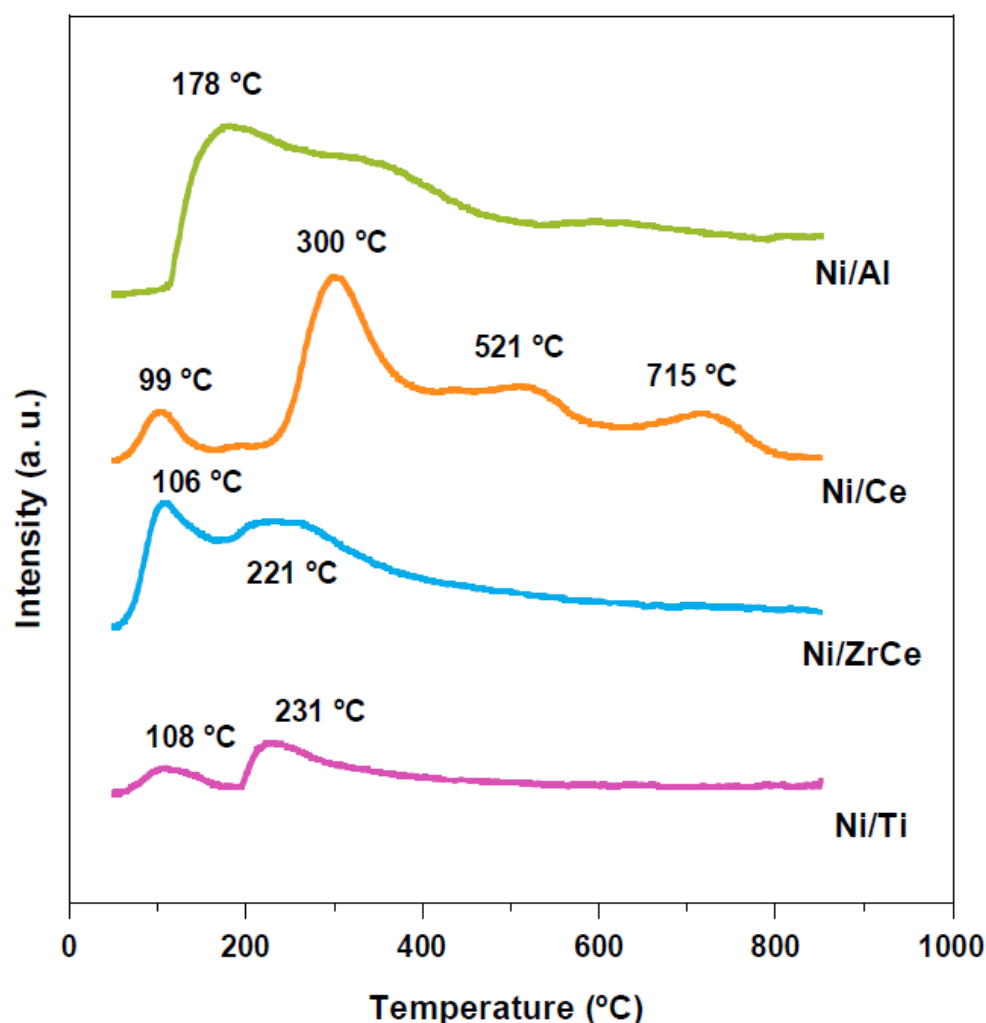

Figure 3. CO_2-TPD profiles of the supported nickel catalysts freshly reduced at 500 °C.

Muroyama et al. [40] recorded a CO_2-TPD profile for a 10 wt.% Ni on alumina catalyst that is very similar to the one corresponding to Ni/Al (Figure 3). The large amount of CO_2 desorbed was related to the high surface area of the catalyst, and the wide temperature range (100–500 °C) within which desorption takes place was related to the presence in the material of a big variety of basic sites with several strengths. As for the amount of CO_2 desorbed, the value recorded with Ni/Al (386 µmol CO_2/$g_{cat.}$) is of the order of magnitude of the values reported in the literature, or even slightly higher than such values reported in the literature (262 µmol CO_2/$g_{cat.}$ and 316 µmol CO_2/$g_{cat.}$ for 10 wt.% Ni [41] and 15 wt.% Ni [66] on alumina catalysts, respectively). As for Ni on the reducible supports, the carbon dioxide adsorption capacity of Ni/Ce (196 µmol CO_2/$g_{cat.}$) is remarkably higher than the one found by Italiano et al. [66] for a 15 wt.% Ni on ceria catalyst (56 µmol CO_2/$g_{cat.}$),

though the specific surface area of the latter was low (21 m^2/g). As a matter of fact, these differences are greatly reduced when the density of basic sites is compared, resulting in 2.1 μmol CO_2/m^2 for Ni/Ce and 2.7 μmol CO_2/m^2 for the 15 wt.% Ni/ceria catalyst. The basic sites' density of a 10 wt.% Ni/ceria catalyst resulted in being 2.0 μmol CO_2/m^2 in the work of Le et al. [34], and this is very close to the value obtained in the present study. These authors also found the presence of medium-strength and strong basic sites in the nickel/ceria sample, whereas the basicity was very low and was only in weak sites in the case of Ni/TiO$_2$, as was also in accordance with findings by other authors [32,43].

Lastly, regarding the ceria–zirconia mixed oxides, Wang et al. [73] found through CO_2-TPD that Ce$_x$Zr$_{1-x}$O$_2$ oxides with x = 0.07, 0.15, 0.25, and 0.8 calcined at 800 °C showed two or three CO_2 desorption events at temperatures within about 250 °C and 550 °C, indicating the presence of medium-strength basic sites in the pristine materials. The basicity increased for samples calcined at lower temperatures (400–600 °C). Pan et al. [39] also detected medium-strength basic sites corresponding to CO_2 desorbed between 250 and 700 °C in a 7 wt.% Ni catalyst supported on Ce$_{0.5}$Zr$_{0.5}$O$_2$ and calcined at 500 °C. Our results with the Ni/ZrCe sample (Figure 3) indicate a lower content of that type of site, as evidenced by the fact that CO_2 desorption is limited to temperatures below 300 °C.

2.2. Catalytic Performance

Figure 4 includes the CO_2 methanation results obtained in the dynamic experiments in which the reaction temperature was raised at a rate of 1 °C/min from 150 to 500 °C, at atmospheric pressure and a constant space velocity of 12 N L CO_2/(g$_{cat.}$·h) (See Section 4.3). Ni/Ce stands out as the most active catalyst of the present study, as it provides the highest CO_2 conversions (Figure 4a) and methane yields (Figure 4b) throughout the whole range of reaction temperatures considered. As for the maximum CO_2 conversion, the following order of decreasing activity results was observed (Figure 4a): Ni/Ce > Ni/ZrCe > Ni/Al ≈ Ni/Ti. A maximum methane yield as high as 84% at about 420 °C is obtained with this sample at the space velocity indicated above (Figure 4b). Ni/ZrCe also exhibits a good catalytic performance, with a maximum methane yield of 78% at around 440 °C. Both Ni/Al and Ni/Ti behave very similarly: maximum methane yield reaches 75% at 468 °C, though Ni/Al provides consistently higher methane yields than Ni/Ti between 150 °C and the temperature at which the maximum value is reached. As can be seen, the differences between the CO_2 conversions and methane yields provided by the several catalysts at intermediate reaction temperatures (between about 275 and 375 °C) are very large. For example, the CO_2 conversions resulting at 350 °C followed the following decreasing order (Figure 4a): 74% (Ni/Ce) > 61% (Ni/ZrCe) > 44% (Ni/Al) > 37% (Ni/Ti). As for the formation of CO, Figure 4c shows that it starts to be measurable at a reaction temperatures above 250 °C, and then it increases continuously as the temperature is raised, reaching yields of 5–6% at 500 °C. It is apparent that there are no significant differences among samples as concerns CO formation.

In order to gain insight into the catalytic activity of the different materials considered in this study, methane formation rates were determined in experiments performed at several reaction temperatures by adjusting the space velocity to operate the reactor under differential conditions. These results are shown in Figure 5.

Methane formation rates expressed per g of catalyst (Figure 5a) essentially reflect the methane yield results obtained at temperatures below 310 °C (Figure 4b). When the rates are normalized to the Ni content (Figure 5b) only Ni/Al gives comparatively increased values because it is the catalyst with the lowest Ni content (see Table 1). Finally, in order to take into account the different Ni dispersions, the reaction rates were also normalized to the metallic Ni surface area. As shown in Figure 5c, this leads to a change in the activity order among samples. Indeed, due to the comparatively low metallic surface area that they expose, Ni/Ti and Ni/ZrCe became the most active catalysts, followed by Ni/Ce and especially Ni/Al, which provide significantly lower activities compared to the rest of the catalyst, particularly as the reaction temperature increases.
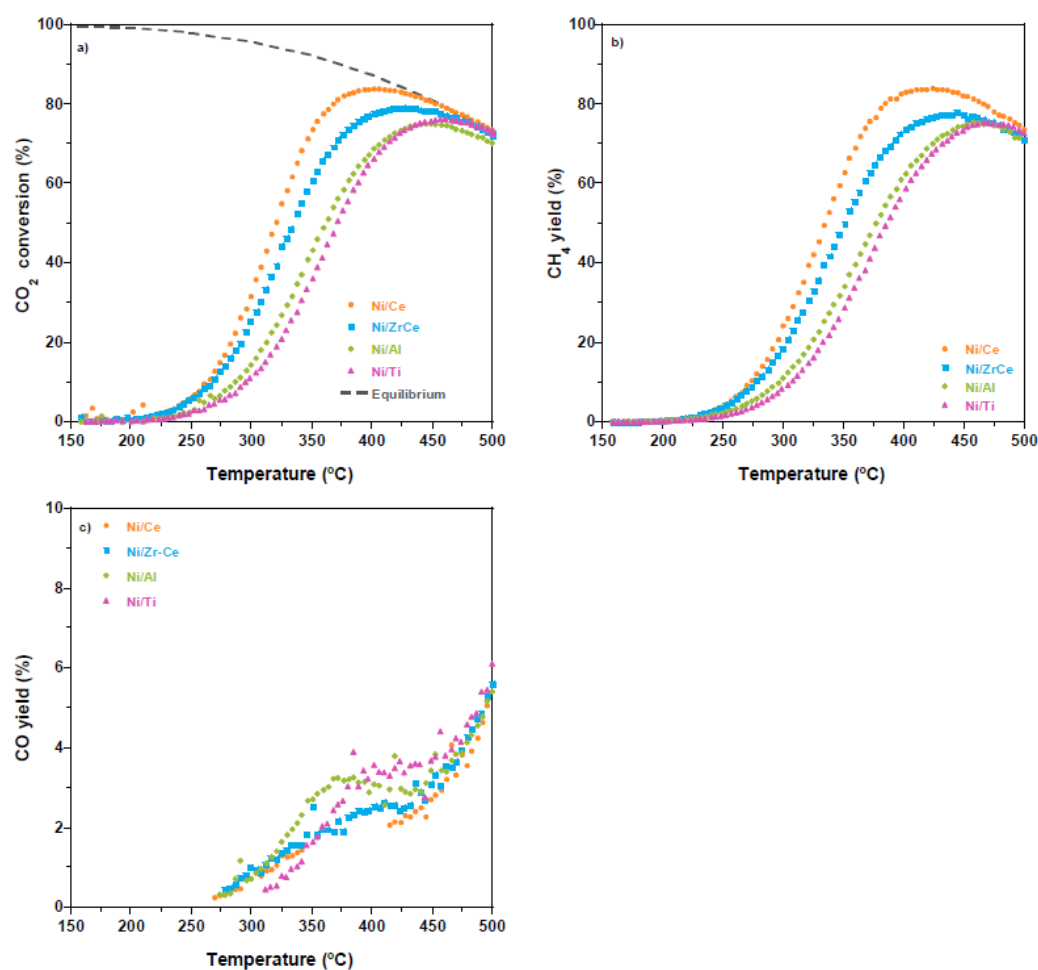
Figure 4. Evolution with reaction temperature of the CO_2 conversion (**a**), CH_4 yield (**b**), and CO yield (**c**) in methanation experiments conducted at space velocity of 12 N L $CO_2/(g_{cat.}\cdot h)$ and H_2/CO_2 molar ratio of 4. Dashed line in (**a**) corresponds to the calculated CO_2 equilibrium conversions.

Apparent activation energies (E_{app}) for methane formation were calculated from the corresponding Arrhenius plots that are presented in Figure 5d. The very good linearity obtained in all the plots is remarkable. In general, there are no big differences among samples regarding this kinetic parameter. Ni/Ti and Ni/ZrCe exhibit very similar apparent activation energies, with values of 80 kJ/mol and 82 kJ/mol, respectively. On the other hand, Ni/Ce shows the highest (89 kJ/mol) and Ni/Al the lowest (78 kJ/mol) values. E_{app} is a macroscopic empirical parameter that can be expressed through the weighted average of the standard-state enthalpies (relative to reactants) of all of the species (intermediates, transition states, and products) involved in the reaction mechanism, each weighted by its generalized degree of rate control (DRC), as shown by Mao and Campbell [74]. The values obtained for Ni/Al, Ni/Ti, and Ni/ZrCe fall within the 78–82 kJ/mol range, so the differences can hardly be considered significant. In contrast, the higher value of 89 kJ/mol calculated for Ni/Ce, in spite of being likely affected by enthalpy effects, could be taken as an indication of a lower intrinsic activity of that catalyst.

Lastly, turnover frequencies of CH_4 formation (TOF_{CH4}) were calculated (see Section 4.3) to measure the specific activity of the catalysts. These results are shown in Figure 6.
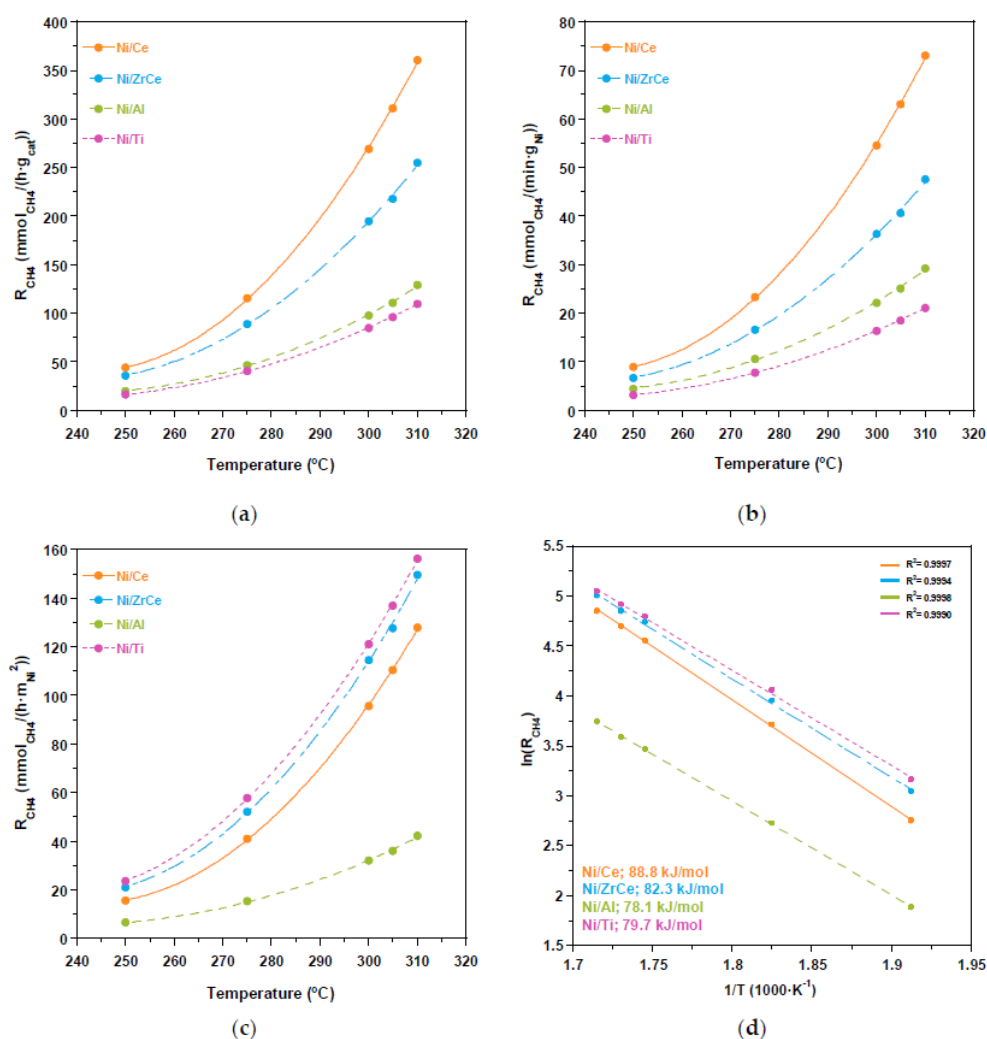
Figure 5. Methane formation rates expressed per g of catalyst (**a**), g of Ni (**b**), and m^2 of Ni (**c**), as obtained from experiments conducted at the temperatures indicated, atmospheric pressure, and H_2/CO_2 molar ratio in the reactor feed of 4. Arrhenius plots based on the methane formation rates normalized to the Ni metallic area (**d**).
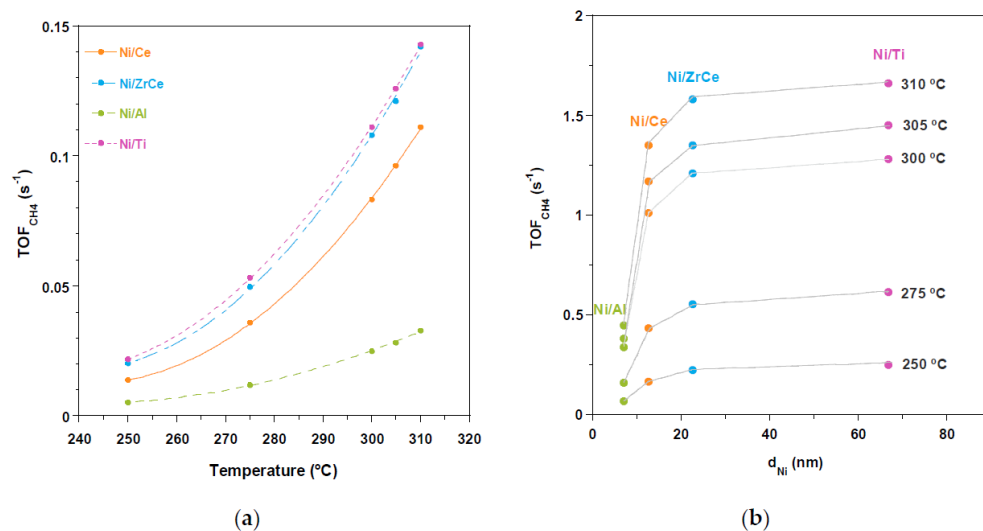

Figure 6. Turnover frequencies of CH_4 formation as functions of the reaction temperature (**a**). Mean metallic Ni particle size derived from CO chemisorption measurements (**b**).

Ni/Ti and Ni/ZrCe exhibit very similar TOF_{CH4} values, which are the highest among the catalysts considered in the present study. Ni/Ce also exhibits a remarkable methanation specific activity that is lower than those of the Ni catalysts supported on titania and ceria–zirconia but higher than that of Ni/Al. This is not in contradiction with the fact that Ni/Ce showed the highest E_{app} value. Indeed, the influence of other factors, such as the pre-exponential factor (A_{app}) of the Arrhenius equation, which is dominated by entropic effects [75], the function dependent on the concentrations of the species kinetically relevant and the density of active sites [76], which are included in the intercept with the ordinate axis in Figure 5d, has to also be taken into account. This means that a combination of these factors may offset the effect of a small increase of the apparent activation energy, resulting in higher reaction rates for Ni/Ce when they are expressed per g of catalyst (Figure 5a) or per g of Ni (Figure 5b). In this regard, the richness of medium-strength basic sites exhibited by Ni/Ce according to the CO_2-TPD results or the influence of the support on the CO_2 methanation kinetics [77] could justify the activity results obtained.

When the metallic Ni particle size is taken into account (Figure 6b), the same trend can be appreciated regardless of the reaction temperature between 250 and 310 °C. As can be seen, TOF_{CH4} increases as the Ni particle size increases, as well, until reaching a sufficiently large value close to the one of Ni/ZrCe (23 nm). At that point, the specific activity seems to become not significantly affected by the Ni particle size. These results point toward the structure sensitivity of the CO_2 methanation reaction over the catalysts considered.

2.3. Operando IR Spectroscopy

Surface IR spectra of the CO_2 methanation reaction over the supported Ni catalysts recorded between 175 and 500 °C are shown in Figures 7–10. In the case of the Ni/Al catalyst (Figure 7), formate, which is considered an important intermediate during the conversion of CO_2 to methane [46], can be distinguished from the beginning of the reaction. Bands at 1379–1397 cm^{-1} (CH bending δ (CH) and symmetric stretching, υ_s (COO-)), 1554–1590 cm^{-1} (asymmetric stretching, υ_{as} (COO-)) [78,79], and 2904 cm^{-1} (υ (CH) stretch, not shown) are attributed to that species. The occurrence of formate species is lower at higher temperatures, which can be due to formates' conversion into carbonate species. Indeed, various carbonate species can be observed: monodentate, bidentate, and hydrogen carbonates with a broad signal between 1652 and 1233 cm^{-1} [80,81]. Monodentate carbonate species are revealed by bands at 1470 cm^{-1} and 1340 cm^{-1} (doubly degenerated υ_{as} stretch). Similarly, hydrogen carbonate species can be detected through the characteristic bands at 1652 cm^{-1} and 1447 cm^{-1} (υ_{as} (CO_3)), whilst the band at 1233 cm^{-1} would correspond to the bending δ (OH). The position of these bands is coincident with the values reported for pure alumina [82]. Next, some weak signals that can be ascribed to organic carbonates are visible at 1817, 1768, 1733, 1202, 1198, and 1255 cm^{-1} [83]. Remarkably, the presence of methoxy species at 400 °C can be proposed as suggested by the bands at 1000 cm^{-1} and 1162 cm^{-1}. The weak bands at 1717 cm^{-1} could be attributed to formaldehyde species [84].

Regarding the Ni/Ce catalyst, the corresponding operando FTIR spectra are shown in Figure 8. CO was observed in the gas phase from the beginning of the reaction. CO could be responsible through the Boudouard reaction for the carbon formation that was observed at temperatures above 350 °C. To be able to complete the measurements with this catalyst, regeneration was carried out by feeding O_2 between each temperature setpoint to remove carbon deposited on the catalyst surface. It should be noted that, in contrast to the catalytic tests, operando FTIR spectroscopy measurements were carried out in the decreasing temperature mode, starting from 500 °C, to decrease the accumulation of adsorbed surface species. However, these conditions are the most favorable for CO formation, which, together with the high activity of the Ni/Ce catalyst (see Figure 4), could have favored carbon formation in the IR reactor cell. However, no significant carbon formation was detected during the catalytic tests, as evidenced by the negative results of the Raman spectroscopy analyses carried out with the used catalysts. As a matter of fact,

carbon formation is not a concern during CO_2 methanation provided that the H_2/CO_2 ratio is maintained to be sufficiently high [85], as in our case.
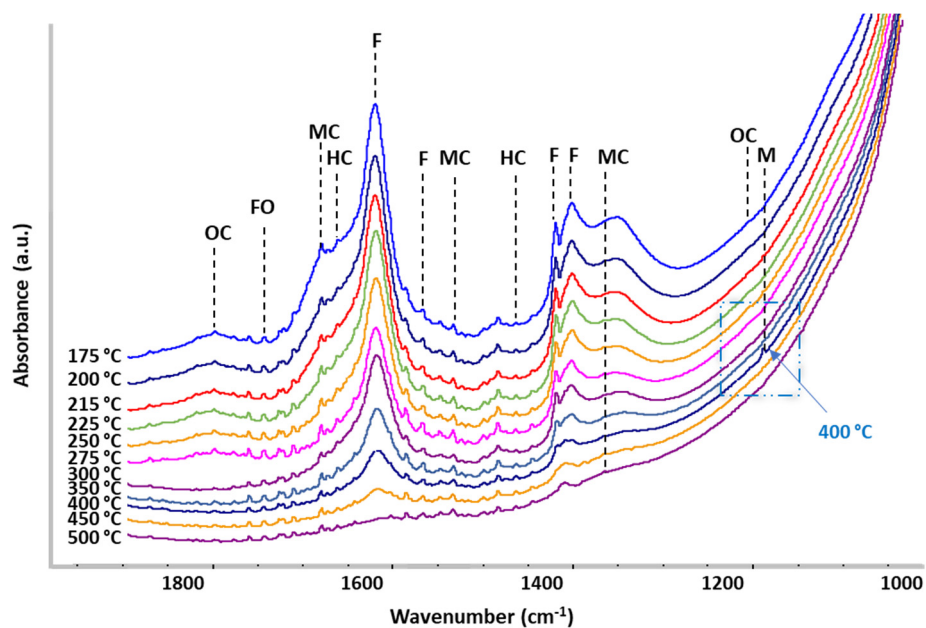

Figure 7. Operando FTIR spectra for CO_2 methanation over the Ni/Al catalyst. Species identification: HC (hydrogen carbonate), MC (monodentate carbonate), BC (bidentate carbonate), OC (organic carbon), F (formate), M (methoxy), FO (formaldehyde).
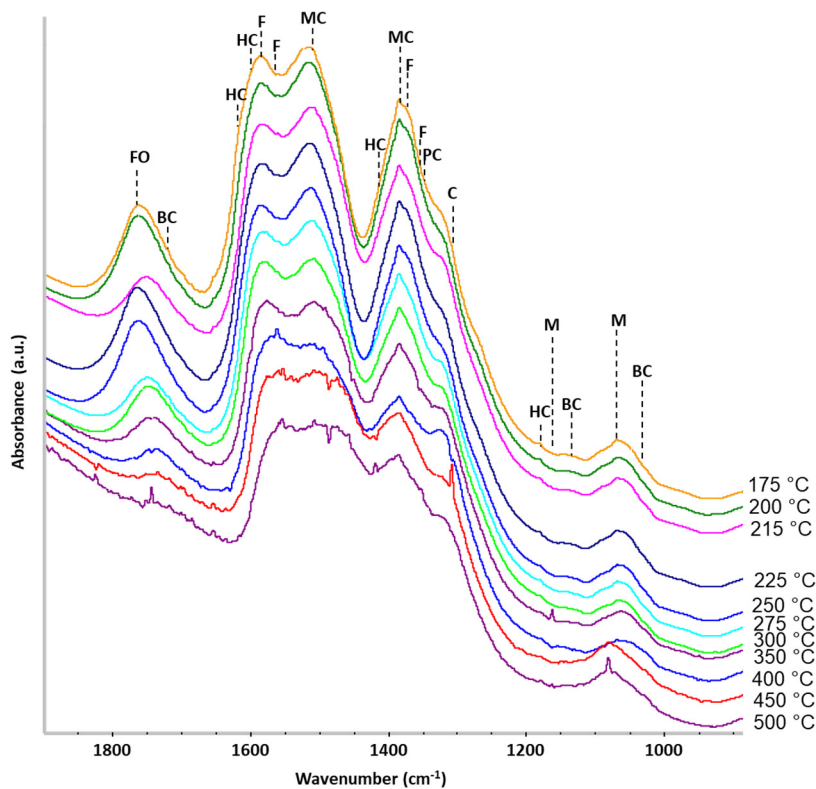

Figure 8. Operando FTIR spectra for CO_2 methanation over the Ni/Ce catalyst. Species identification: HC (hydrogen carbonate), MC (monodentate carbonate), BC (bidentate carbonate), PC (polydentate carbonate), F (formate), M (methoxy), FO (formaldehyde), C (carboxylate).

Figure 9. Operando FTIR spectra for CO_2 methanation over the Ni/ZrCe catalyst. Species identification: HC (hydrogen carbonate), MC (monodentate carbonate), BC (bidentate carbonate), PC (polydentate carbonate), F (formate), M (methoxy), FO (formaldehyde), and C (carboxylate).
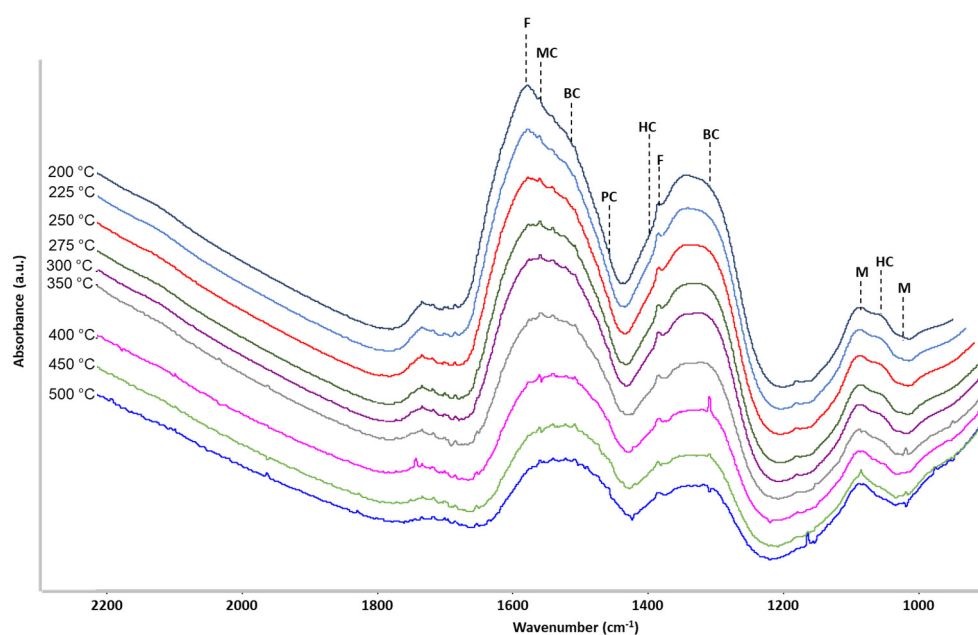

Figure 10. Operando FTIR spectra for CO_2 methanation over the Ni/Ti catalyst. Species identification: HC (hydrogen carbonate), MC (monodentate carbonate), BC (bidentate carbonate), PC (polydentate carbonate), F (formate), M (methoxy), FO (formaldehyde), and C (carboxylate).
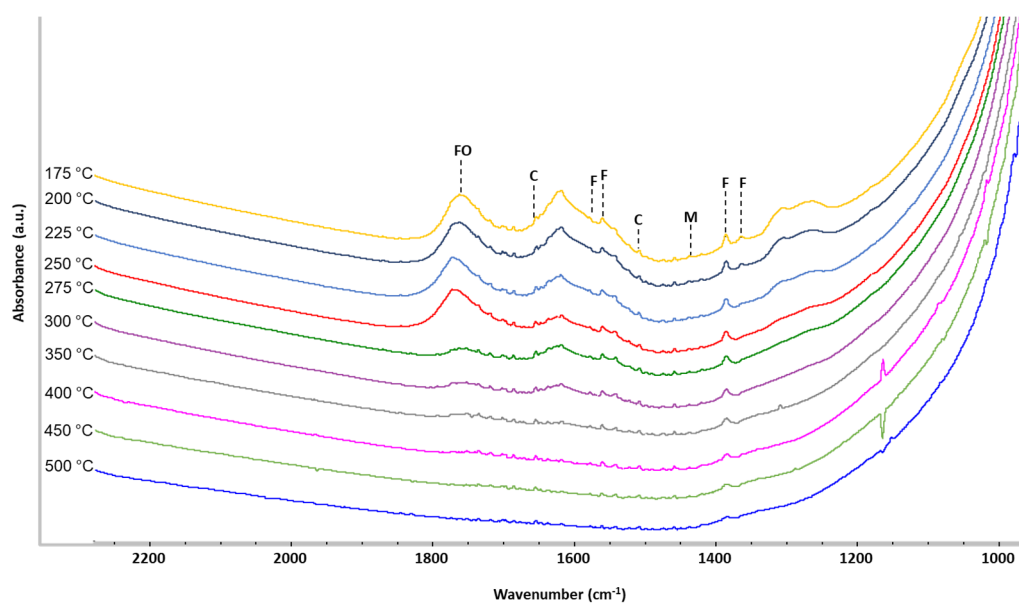
As can be seen in Figure 8, several bands corresponding to formate species can be distinguished, such as the υ_{as} (COO-) mode at 1583 cm^{-1} and 1560 cm^{-1} that can be ascribed to species formed on Ce^{3+} sites of the partly reduced ceria support [86,87]. Furthermore, small symmetric stretching bands of formate species can be detected at 1355 cm^{-1}, and the corresponding δ (CH) at 1375 cm^{-1} [88,89]. Similar to the case of Ni/Al catalysts, various bands corresponding to methoxy species are observed in the spectra at 1160 (rocking r(CH$_3$)), 1100, 1060, and 1000 cm^{-1}, owing to the stretching vibration υ (C-O). The band near 1100 cm^{-1} is more sensitive to the nature of the surrounding cations on the surface, while the band near 1060 cm^{-1} is more complex and broader. In our case, weak

bands of these species can be seen at 1162 cm^{-1} (spectra recorded at 500, 350, and 300 °C) and 1062–1080 cm^{-1} (spectra recorded at 500, 450, and 350 °C) [90–92]. In the case of pure ceria, bands due to the methoxy species on top (1106 cm^{-1}), double bridging (1080 cm^{-1} and 1050 cm^{-1}), and triple bridging (1012 cm^{-1}) have been reported and associated with coordinatively unsaturated surface sites [93].

A great variety of carbonate species can also be distinguished in the surface spectra of the Ni/Ce catalyst. Small bands of hydrogen carbonate species are observed at temperatures between 350 and 500 °C at 1617, 1599, and 1416 cm^{-1} for the vibrational stretching mode, υ (CO_3) [92]; 1217 cm^{-1} for deformation, δ (OH) [94]; and 815 cm^{-1} for out-of-plane deformation, π (CO_3) [91]. In addition, characteristic bands of bidentate carbonates can be visualized at 1576, 1290, 1013, and 856 cm^{-1}, corresponding to the stretching modes υ_{as} (CO_3) for the first two bands, υ_s (CO_3) for the following, and π (CO_3) for the last [88,91,92,95]. With respect to the "bridged" carbonates, small bands are observed at 1736 cm^{-1} and 1133 cm^{-1} of in the vibrational mode υ_{as} (CO_3). Bands of polydentate carbonate are evident at ~1530, 1353 cm^{-1} (υ_{as} (CO_3)), and 854 cm^{-1} (π (CO_3)) [91,92]. The bands at 1504 cm^{-1} (υ_{as} (CO_3)) [95] and 1384 cm^{-1} [96] are attributed to monodentate carbonates. With regard to carboxylates, weak bands could be assigned at 1307 cm^{-1} [86] and 1561 cm^{-1} [81]. On the other hand, bands at 1765 cm^{-1} are observed in the runs conducted at 225, 300, 350, and 450 °C, which could be attributed to formaldehyde species [97].

As for the Ni/ZrCe catalyst, the corresponding operando FTIR spectra are shown in Figure 9. Bands corresponding to formate species on Zr^{4+} sites are observed at 1575 cm^{-1} and 1383 cm^{-1} (υ (OCO)), while the band at 1560 cm^{-1} is ascribed to formate on Ce^{3+} [87,98]. On the other hand, bands at 1546 cm^{-1} and 1306 cm^{-1} can be assigned to the vibration mode υ_{as} (COO-) of bidentate carbonates, together with the π (CO_3) mode at 871 cm^{-1}. In contrast, very weak bands are observed at 1520 and ~1330 cm^{-1}, which correspond to the υ_{as} (COO-) mode of monodentate carbonate. Finally, bands are displayed at 1458 cm^{-1} and 852 cm^{-1} that are assigned to the υ_s (COO-) and π (CO_3) modes, respectively, of polydentate carbonates [95,99]. With respect to the methoxy species, it is possible to see some small characteristic bands just above 1100 cm^{-1} that are associated with the stretching vibration, υ (C-O), of linearly coordinated methoxy on coordinatively unsaturated Zr^{4+} cations. In addition, a band at 1083 cm^{-1} is assigned to the double bridging species on Ce^{3+}, while the shoulder at 1055 cm^{-1} is due to methoxy bridged over Ce^{4+} cations neighboring an oxygen vacancy [100].

Finally, Figure 10 includes the spectra resulting from the CO_2 methanation on the Ni/Ti catalyst. The following bands were observed corresponding to formate species on Ti^{4+} sites: 1576 cm^{-1}, 1560 cm^{-1}, 1384 cm^{-1} and 1360 cm^{-1}, and 1384 cm^{-1}, attributed to the υ_{as} (COO-), δ(CH), and υ_s (COO-) vibrational modes, respectively [84,101–104]. Furthermore, formaldehyde was detected as an adsorbed species at 1755 cm^{-1} [103]. As for carbonates, several weak bands in the range 1600–1200 cm^{-1} can be likely ascribed to those species (being difficult and not really useful to distinguish the exact geometry of the different vibrators). The most relevant peaks in the region 1650–1500 cm^{-1} are probably due to carboxylates.

As concerns methoxy species on Ni/Ti, some characteristic bands can be guessed in the 1500–1000 cm^{-1} domain, where we expect the vibration of molecularly adsorbed methanol modes δ(CH_3), δ(H-O-C), and υ(C-O) at 1467, 1370 and 1121, and 1033 cm^{-1} respectively [101,103,105]. Bands at 1436 (C-H bending) and 1163, 1104, and 1071 cm^{-1} (C-O stretches), can be ascribed to the dissociatively chemisorbed methoxy species on Ti^{4+} [105].

3. Discussion

The results presented in the preceding section clearly show the remarkable influence of the support on the performance of nickel catalysts for the methanation of CO_2, in line with previous works on this topic [32–37,43]. The differences in performance found are likely related to the support nature itself and its effects on the nickel precursor reducibility, metallic

dispersion, catalysts basic properties, and surface reactivity toward the activation of CO_2, as suggested by the information provided by the physicochemical characterization results.

It is important to remark that differences in catalytic performance lie more in activity than selectivity since CO production has been found to be low, limited to the highest reaction temperatures considered, and very similar on the four investigated catalysts (Figure 4c). Apparent activation energies for methanation have also resulted in being rather similar, and operando FTIR spectroscopy measurements have evidenced the presence of almost the same type of adsorbed species during the course of the reaction regardless of the support nature. The differences in the carbonate species' intensities, which are much higher in the ceria and ceria–zirconia supports, are due to the greater basicity of those oxides. In principle, these results indicate that the different behavior of the catalysts may be due to differences in the abundance and nature of the active sites and not to significant changes in the reaction mechanism depending on the support.

From a practical viewpoint, the nickel catalyst supported on ceria (Ni/Ce) is clearly the most interesting one since it has provided a comparatively high methanation rate in terms of both catalyst weight (Figure 5a) and nickel content (Figure 5b), which are parameters that are strongly related to the reactor size and catalyst cost. This catalyst seems to have a good balance between active sites associated with metallic nickel and the support through either the support itself or the metal–support interface. Indeed, as concerns nickel sites, Ni/Ce exhibits a much higher metallic surface area compared to nickel supported on the other two reducible supports (see Table 1), i.e., ceria–zirconia mixed oxide (Ni/ZrCe) and titania (Ni/Ti). This fact, together with the reasonably high specific surface area, is expected to also have a positive effect on the extension of the metal–support interface. In this regard, oxygen vacancies created on the ceria surface during the activation of the catalyst by H_2-reduction can be refilled throughout reaction by CO_2, which becomes activated and partially hydrogenated by hydrogen atoms adsorbed on neighboring metallic Ni particles, thus evolving to form reaction intermediates and final products. The proximity and compatibility between active sites have been found to be essential for the CO_2 hydrogenation reactions [106]. On the other hand, the CO_2-TPD results (Figure 3) have shown that Ni/Ce has a rich surface, as concerns the presence of medium-strength basic sites capable of adsorbing, and presumably activating the CO_2 molecule, which has been related to high methanation activity [39–43]. The operando FTIR results obtained with Ni/Ce sustain this interpretation (Figure 8) because a variety of species have been identified related to CO_2 adsorption (hydrogen carbonates, monodentate carbonates, bidentate carbonates, and polydentate carbonates). Although these species differ in reactivity, the fact is that the presence of formates, carboxylates, and methoxy species, whose formation requires the assistance of activated hydrogen, provides evidence that Ni/Ce meets the conditions to have a good activity.

Following this reasoning, it could be argued that such a favorable balance between active sites is not achieved with the rest of the catalysts investigated in the present work. In the case of Ni/ZrCe catalyst, the CO_2-TPD results show the presence of few medium-strength basic sites; in addition, the Ni surface area is about half that of Ni/Ce, thus resulting in a lower number of active sites, even though it shows a reasonable activity. As for Ni/Ti, medium-strength basic sites are absent, and the catalyst shows a low specific surface area and Ni dispersion, resulting in low activity compared to the other nickel catalysts supported on reducible metal oxides.

Regarding the Ni/Al catalyst, the results are somewhat surprising. In principle, this catalyst exhibits the highest metallic dispersion and high specific surface area and the presence of medium-strength basic sites. In addition, operando FTIR spectroscopy measurements have evidenced the presence of species associated with CO_2 adsorption and their partial hydrogenation (such as hydrogen carbonates and formates). In spite of these good features, its activity in terms of catalyst weight and Ni loading is only slightly higher than that of Ni/Ti and much lower than the those of Ni/Ce and Ni/ZrCe. An obvious difference among these catalysts is that the support of Ni/Al is non-reducible

and relatively acid. It could be speculated that, as a result, the cooperative effect between metallic Ni and the sites linked to the support is less efficient in this case, perhaps due in part to the absence of surface oxygen vacancies. It is worth mentioning in this regard that Ni/Al has provided much lower TOF_{CH4} values than the rest of the catalysts (see Figure 6). Of course, this magnitude should be considered carefully since its calculation was performed based on the metallic surface area as a measure of the active sites. In addition, chemisorption may be an unsuitable characterization technique for catalysts supported on reducible oxides due to the well-known effects associated with strong metal–support interaction phenomena. Bearing these limitations in mind, it could be concluded that using as support of Ni a reducible metal oxide that is capable of developing basicity associated with medium-strength basic sites, and a suitable balance between metallic sites and centers linked to the support (e.g., oxygen vacancies) through the metal–support interface leads to high CO_2 methanation activity.

As for the Ni particle size, it seems also to play a role since the results shown in Figure 6 suggest that the reaction is structure sensitive on Ni catalysts. In this regard, the specific activity increases with the particle size until a sufficiently large value of about 25–30 nm is reached, from which this parameter seems to lose importance.

Finally, although studying the CO_2 methanation mechanism is beyond the aim of this work, the results obtained by operando FTIR spectroscopy may suggest that, for the catalysts under consideration, it follows the formate pathway [45,46,107]. As schematized in Figure 11, CO_2 is first adsorbed onto surface hydroxyls and oxygen sites to form hydrogen carbonates and monodentate and bidentate carbonates. These carbonates readily react, being hydrogenated by H atoms chemisorbed on the nearby metallic Ni particles to form formate species. Afterward, a series of hydrogenation reactions take place that convert formates into formaldehyde species that are further hydrogenated to methoxy species and finally methane.
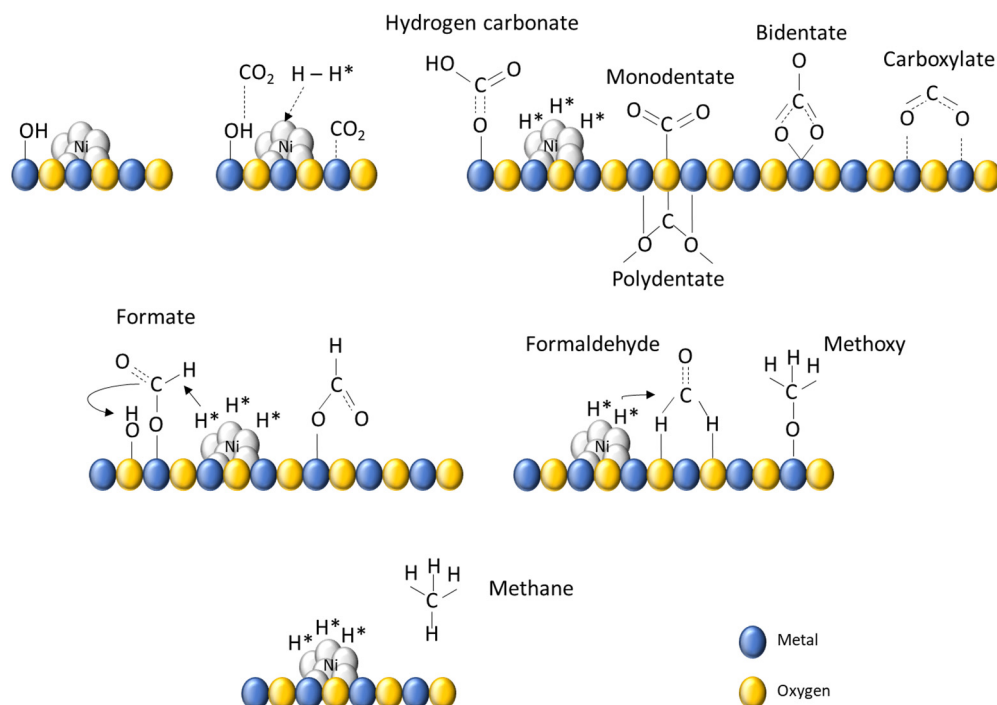

Figure 11. Scheme illustrating the formate pathway for CO_2 methanation on supported Ni catalysts.

4. Materials and Methods

4.1. Catalysts Preparation

A series of Ni catalysts were prepared by the incipient wetness impregnation method. Different commercial supports were used: γ-Al_2O_3 from Alfa Aesar (Ward Hill, MA, USA),

ZrO_2-CeO_2 supplied by Tecnan-Lurederra (Los Arcos, Navarra, Spain), and TiO_2 P-25 provided by Evonik Degussa (Essen, Germany). These materials were referred to as Al, ZrCe, and Ti, respectively. In addition, CeO_2 support (denoted as Ce) was prepared in the laboratory by thermal decomposition of cerium nitrate ($Ce(NO_3)_3 \cdot 6H_2O$, Merck, Darmstadt, Germany) at 500 °C for 4 h in air atmosphere. All supports were manually grinded and sieved, and the solids fraction having a particle size within the 100–200 μm range was selected for catalyst preparation in order to minimize possible internal concentration and temperature gradients. Before impregnation, they were calcined in a muffle furnace at 500 °C for 4 h, using a heating rate of 2 °C/min, to remove volatiles and adsorbed impurities. Specific surface areas of the calcined solids used as supports were as follows: 220 m^2/g (γ-Al_2O_3), 112 m^2/g (CeO_2), 110 m^2/g (ZrO_2-CeO_2), and 59 m^2/g (TiO_2). High-purity $Ni(NO_3)_2 \cdot 6H_2O$ (Acros Organics, Geel, Belgium) was used as Ni precursor and was dissolved in deionized water at room temperature. The exact amounts for preparing the aqueous solutions were determined in accordance with the water pore volume measured beforehand for each support and the nominal Ni content of the catalysts that was fixed at 10 wt.%. After impregnation, the solids were dried overnight in an oven at 110 °C and then calcined at 500 °C for 4 h. The four final catalysts were named Ni/Al, Ni/ZrCe, Ni/Ti, and Ni/Ce.

4.2. Physicochemical Characterization

Elemental analysis was performed by optical emission spectrophotometry combined with inductively coupled plasma (ICP) to determine the actual content of Ni in each catalyst. The analyses were conducted by Servicio de Análisis Químico of the Servicios de Apoyo a la Investigación (SAI) of the University of Zaragoza (Zaragoza, Spain), using a Thermo Elemental IRIS INTREPID RADIAL spectrophotometer.

Textural parameters were derived from nitrogen adsorption–desorption measurements at the N_2 saturation temperature at atmospheric pressure (77 K). Analyses were carried out in a static volumetric analyzer (Micromeritics Gemini V 2380), in which the sample was previously treated under N_2 gas flow for 2 h at 200 °C. The specific surface area (S_{BET}) was calculated according to the Brunauer–Emmett–Teller (BET) method, and the pore size distribution and average pore size were determined by the Barrett–Joyner–Halenda (BJH) method.

Hydrogen temperature-programmed reduction (H_2-TPR) analyses were carried out in an AutoChem II 2920 (Micromeritics) analyzer equipped with a thermal-conductivity detector (TCD) to determine the hydrogen consumption. The samples were placed in a U-tube quartz reactor, and H_2-TPR was performed by feeding 75 N mL/min of a gas containing 5 vol. % H_2 in Ar, and the temperature was increased from 40 to 930 °C at a controlled rate of 5 °C/min. Metallic nickel dispersion (D_{Ni}) and surface area (S_{Ni}) were determined using the same automatic analyzer through CO pulse chemisorption measurements at a temperature of 40 °C, using 50 N mL/min of 10 vol. % CO in He as analysis gas. Prior to measurements, the samples were reduced under a H_2 gas flow for 3 h at 500 °C. Once the volume of CO chemisorbed per g of Ni is experimentally determined under given conditions (in this case, 273,15 K, and 1 atm), the number of chemisorbed CO molecules can be easily calculated. Assuming a chemisorption stoichiometry of 1 CO molecule per exposed Ni atom, the number of metallic Ni atoms exposed on the surface per g of Ni is obtained. The metallic surface area (S_{Ni}) expressed in m^2/g_{Ni} can be obtained simply multiplying the number of exposed Ni atoms per g of Ni by the mean area occupied by a Ni atom (A_{Ni}, 6.33 × 10^{-20} m^2/Ni atom) [108,109]. As for the metallic Ni dispersion (D_{Ni}), it was calculated according to its definition as the ratio between the number of exposed metallic Ni atoms per g of catalysts or g of Ni and the corresponding total number of Ni atoms.

After the chemisorption measurements, the degree of reduction of nickel (DOR_{Ni}), i.e., the fraction of the nickel present in the catalyst that was effectively reduced after the pretreatment under hydrogen, was determined in situ, using the same equipment

(AutoChem II 2920). For that purpose, samples were heated from 40 to 430 °C, under flowing He, and then pulses of 10 vol. % O_2 in He were fed until achieving the end of oxygen consumption. The amount of oxygen consumed allows us to determine the amount of both surface and bulk reduced Ni atoms, assuming that metallic Ni is quantitatively converted into NiO [58]. This allows us to calculate DOR_{Ni} according to its definition as the ratio between the number of reduced Ni atoms per g of catalyst or g of Ni and the corresponding number of total (reduced and non-reduced) Ni atoms in the sample.

The nickel average particle diameter (d_{Ni}) (defined as the cube root of the volume) was calculated from the metallic surface area and DOR_{Ni} by assuming that the metallic particles are spherical (Ni/Ce, Ni/ZrCe, and Ni/Ti) or hemispherical (Ni/Al) and that the unreduced nickel phase is separated from the reduced particles. This distinction is made to take into account the different interaction that can be established in each case between the metal and the support in the catalyst precursor [58,59,108].

Temperature-programmed desorption of CO_2 (CO_2-TPD) was employed to characterize catalysts basicity and CO_2 adsorption capacity. Measurements were conducted in the abovementioned Micromeritics AutoChem II 2920 (Micromeritics) apparatus. The sample (0.065 g) was loaded on a quartz wool plug placed inside a U-shaped quartz reactor. Afterward, the catalyst was reduced under a H_2 gas flow (60 N mL/min) for 3 h at 500 °C; then the reactor was allowed to cool to 50 °C while the flowing gas was switched to He. Once the temperature was stabilized, the sample was exposed to CO_2 (10 vol. % in He) at total flow rate of 50 N mL/min for 1 h. Next, the sample was exposed to a He flow for 30 min to sweep away the weakly adsorbed (physisorbed) CO_2. Lastly, chemisorbed CO_2 desorption was conducted by increasing the temperature from 50 to 850 °C, using a heating rate of 20 °C/min. Desorbed CO_2 was analyzed by means of thermal conductivity (TCD) detector.

Powder X-ray diffraction (XRD) analyses were conducted by the SAI of the University of Zaragoza. The diffraction patterns were recorded using a Rigaku D-Max/2500 diffractometer in the 2θ angle range of 5°–95°. The diffractometer was equipped with a Ni-filtered Cu anode and used a graphite monochromator to select a radiation source with a wavelength of 1.5418 Å. The X-ray source was operated at 40 kV and 80 mA, with a step of 0.03° and a time constant of 1 s/step. The identification of the crystalline phases was made by comparison of the XRD patterns of the samples against standard diffraction patterns from the Joint Committee on Power Diffraction Standards (JCPDSs-2000) database.

4.3. Catalytic Tests

The catalytic activity tests of the CO_2 methanation reaction were conducted in a laboratory-scale continuous flow fixed-bed tubular quartz reactor (10 mm ID), under atmospheric pressure. The catalytic bed was typically composed of a physical mixture of 0.1 g of the as-prepared catalyst and 0.9 g of commercial α-Al_2O_3 (Strem Chemicals, Newburyport, MA, USA) used as inert filler, resulting in a bed of 6 mm in length. A thermocouple was inserted inside the bed, fixing its position in such a way that its lower end was placed inside the bed but just at its exit. This thermocouple was connected to a programmable temperature controller that regulated the power of the oven in which the reactor was vertically positioned, using stainless steel tubing and fittings. High-purity H_2 and CO_2 gases were fed into the reaction system by means of Bronkhorst (Ruurlo, The Netherlands) mass flow controllers in order to have a gas feeding mixture of 100 N mL/min with a H_2/CO_2 molar ratio of 4, and an additional flow of 12 N mL/min of N_2 used as internal standard for the chromatographic analyses. These conditions resulted in a space velocity that referred to the catalyst weight ($F_{CO2(in)}/W_{cat.}$) of 12 N L CO_2/($g_{cat.}$·h) that was fixed in all dynamic experiments in which the reaction temperature was raised at a rate of 1 °C/min from 150 to 500 °C. Some experiments were performed at constant reaction temperature within the 250–310 °C range and adjusting the space velocity to obtain CO_2 conversions below 10%. The results from these experiments allowed us to calculate reaction rates and turnover frequencies under the assumption of a gradientless plug flow

isothermal differential reactor. Prior to the activity tests, the catalysts were reduced in situ at 500 °C for 12 h, under 60 N mL/min of H_2. The composition of the outlet gas was analyzed online after removing the water produced in a condenser cooled via the Peltier effect. A gas chromatograph (Agilent 490 MicroGC) equipped with two chromatographic columns (CP-Molsieve 5A and CP-PoraPLOT U) and thermal conductivity detectors (TCDs) was used. Carbon balance was satisfied within ± 5%, which is of order of the experimental error. No significant carbon formation took place during the catalytic tests, as judged from the absence of characteristic carbon signals in the Raman spectra performed on the used catalysts.

CO_2 conversion (X_{CO2}), CH_4 selectivity (S_{CH4}) and yield (Y_{CH4}), and CO selectivity (S_{CO}) and yield (Y_{CO}) were calculated as functions of the corresponding inlet ($F_{(in)}$) and outlet ($F_{(out)}$) molar flow rates according to the following equations:

$$X_{CO2}(\%) = \frac{F_{CO2(in)} - F_{CO2(out)}}{F_{CO2(in)}} \cdot 100, \tag{1}$$

$$S_{CH4}(\%) = \frac{F_{CH4(out)}}{F_{CO2(in)} - F_{CO2(out)}} \cdot 100, \tag{2}$$

$$Y_{CH4}(\%) = \frac{F_{CH4(out)}}{F_{CO2(in)}} \cdot 100, \tag{3}$$

$$S_{CO}(\%) = \frac{F_{CO(out)}}{F_{CO2(in)} - F_{CO2(out)}} \cdot 100, \tag{4}$$

$$Y_{CO}(\%) = \frac{F_{CO(out)}}{F_{CO2(in)}} \cdot 100, \tag{5}$$

On the other hand, from the results obtained when the reactor was operated under differential regime, the CO_2 consumption ($-R_{CO2}$) and CH_4 (R_{CH4}) and CO (R_{CO}) formation reaction rates were calculated as follows:

$$-R_{CO2} = \left(F_{CO2(in)}/W_{cat.}\right) \cdot X_{CO2} \tag{6}$$

$$R_{CH4} = \left(F_{CO2(in)}/W_{cat.}\right) \cdot Y_{CH4}, \tag{7}$$

$$R_{CO} = \left(F_{CO2(in)}/W_{cat.}\right) \cdot Y_{CO}, \tag{8}$$

Finally, the turnover frequency of CH_4 formation (TOF_{CH4}) was calculated as the number of CH_4 molecules formed per metallic nickel surface atom per second, assuming that the exposed nickel atom is the active site for CO_2 methanation, according to the following:

$$TOF_{CH4} = \frac{R_{CH4} \cdot N_A \cdot A_{Ni}}{S_{Ni}}, \tag{9}$$

where R_{CH4} is the rate of CH_4 formation following Equation (7) in mol $CH_4/(s \cdot g_{Ni})$, N_A is the Avogadro's number (6.023×10^{23} molecules/mol), and S_{Ni} and A_{Ni} are the metallic Ni surface area and the mean area occupied by an exposed Ni atom defined in Section 4.2.

4.4. Operando IR Spectroscopy

The infrared (IR) operando system employed is composed of four main parts: the spectrometer, the reactor cell, the gas distribution system and the gas analyzers. A detailed description of the setup can be found elsewhere [110,111]. The IR reactor cell was connected to the operando gas system that includes mass flow controllers for feeding the gases into the lines. Two gas mixtures, one used for in situ activation (reduction) of the catalyst and another for conducting the CO_2 hydrogenation tests, could be prepared

and sent independently to the reactor cell. Analyses of the gas stream compositions were performed by means of a Quadrupole Mass Spectrometer (QMS) (Pfeiffer Omnistar GSD 301), while complementary information on the gas phase was obtained by IR spectroscopy through a gas microcell. Surface IR spectra were collected with a Thermo Scientific Nicolet 6700 spectrometer, equipped with a Mercury–Cadmium–Telluride (MCT) IR detector, at the maximum speed of a spectrum every 50 ms. In order to ameliorate the signal-to-noise ratio, 16 scans were collected per spectrum at an optical resolution of 4 cm^{-1}. As for the QMS analyses, the time resolution obtained was 1 s. To conduct the experiments in the IR cell, around 20 mg of each catalyst sample, initially in the form of a thin powder, was pressed into a self-supported disc (2 cm^2 area, 10 mg·cm^{-2}) to make a pellet that was placed inside the cell. Prior to the test, all catalysts were activated through in situ reduction at 500 °C for 12 h under a flow of 10 N mL/min H$_2$ and 12.4 N mL/min Ar. Experiments were carried out at atmospheric pressure, and initial temperature of 500 °C that was diminished to 175 °C under reaction flow in a controlled way. The total flow rate used throughout the experiments was 22.4 N mL/min, feeding 10 N mL/min of H$_2$, 2.5 N mL/min of CO$_2$ (H$_2$/CO$_2$ molar ratio of 4) and Ar (balance).

5. Conclusions

A series of Ni catalysts supported on alumina (Ni/Al), ceria (Ni/Ce), ceria–zirconia (Ni/ZrCe), and titania (Ni/Ti) were prepared, characterized, and tested in the methanation of CO$_2$. The results showed that the nature of the support has important effects on the catalytic performance, mainly on the catalytic activity, whilst all the investigated catalysts were stable and very selective toward methane formation. Ni/Ce has stood out as the most active catalyst, providing the highest CO$_2$ conversions, methane yields, and reaction rates expressed per g of catalyst or g of nickel. The good performance of this catalyst is attributed to the presence of a suitable balance between active sites, as suggested by the results provided by CO$_2$-TPD and operando FTIR characterization, as well as by the catalytic tests. In this regard, medium-strength basic sites associated with the support are capable of adsorbing, and presumably activating, CO$_2$, whereas metallic Ni sites catalyze the hydrogen-assisted evolution of activated CO$_2$ (e.g., in the form of hydrogen carbonates or carbonates) to partially hydrogenated intermediates such as formate and methoxy species that finally yield methane. Formate species on sites corresponding to the partially reduced support were detected on Ni/Ce, thus indicating that the sites associated with the interface between the support and the Ni particles could play a key role. This overall picture is significantly different compared to the cases of Ni/Al and Ni/Ti, which were the least active catalysts of the series. It should be noted that alumina is non-reducible, whereas CO$_2$-TPD evidenced the absence of medium-strength sites on Ni/Ti. Lastly, Ni/ZrCe provided good results, though the activity was lower than that of Ni/Ce, probably due to a lower abundance of active sites or to a less favorable balance between the different types of centers. The operando FTIR results were in accordance with the occurrence of the methanation of CO$_2$ through the formate route on the four investigated nickel catalysts. The relative intensities of the signals are influenced by the basic strength and reducible character of the support in qualitative agreement with the activities exhibited by the catalysts.

Conflicts of Interest: The authors declare no conflict of interest. The funders had no role in the design of the study; in the collection, analyses, or interpretation of data; in the writing of the manuscript; or in the decision to publish the results.

References

1. Pearce, B.B.; Twigg, M.V.; Woodward, C. Methanation. In *Catalyst Handbook*, 2nd ed.; Twigg, M.V., Ed.; Manson Publishing: Frome, UK, 1996; pp. 340–383.
2. Seglin, L.; Geosits, R.; Franko, B.R.; Gruber, G. Survey of Methanation Chemistry and Processes. In *Methanation of Synthesis Gas. Advances in Chemistry Vol. 146*; Seglin, L., Ed.; American Chemical Society: Washington, DC, USA, 1975; pp. 1–30.
3. Kopyscinski, J.; Schildhauer, T.J.; Biollaz, S.M.A. Production of synthetic natural gas (SNG) from coal and dry biomass—A technology review from 1950 to 2009. *Fuel* **2010**, *89*, 1763–1783. [CrossRef]
4. Duret, A.; Friedli, C.; Maréchal, F. Process design of Synthetic Natural Gas (SNG) production using wood gasification. *J. Clean Prod.* **2005**, *13*, 1434–1446. [CrossRef]
5. Gao, J.; Liu, Q.; Gu, F.; Liu, B.; Zhong, Z.; Su, F. Recent advances in methanation catalysts for the production of synthetic natural gas. *RSC Adv.* **2015**, *5*, 22759. [CrossRef]
6. Rönsch, S.; Schneider, J.; Matthischke, S.; Schlüter, M.; Götz, M.; Lefebvre, J.; Prabhakaran, P.; Bajohr, S. Review on methanation—From fundamentals to current projects. *Fuel* **2016**, *166*, 276–296. [CrossRef]
7. Gong, J.; English, N.J.; Pont, D.; Patzke, G.R.; Protti, S.; Zhang, T. Power-to-X: Lighting the Path to a Net-Zero-Emission Future. *ACS Sustain. Chem. Eng.* **2021**, *9*, 7179–7181. [CrossRef]
8. Incer-Valverde, J.; Patiño-Arévalo, L.J.; Tsatsaronis, G.; Morosuk, T. Hydrogen-driven Power-to-X: State of the art and multicriteria evaluation of a study case. *Energy Convers. Manag.* **2022**, *266*, 115814. [CrossRef]
9. Bargiacchi, E.; Candelaresi, D.; Spazzafumo, G. Power to methane. In *Power to Fuel. How to Speed Up a Hydrogen Economy*; Spazzafumo, G., Ed.; Academic Press—Elsevier: London, UK, 2021; pp. 75–101.
10. Bargiacchi, E. Power-to-Fuel existing plants and pilot projects. In *Power to Fuel. How to Speed Up a Hydrogen Economy*; Spazzafumo, G., Ed.; Academic Press—Elsevier: London, UK, 2021; pp. 211–237.
11. Ghaib, K.; Ben-Fares, F.-Z. Power-to-Methane: A state-of-the-art review. *Renew. Sustain. Energy Rev.* **2018**, *81*, 433–446. [CrossRef]
12. Navajas, A.; Mendiara, T.; Gandía, L.M.; Abad, A.; García-Labiano, F.; de Diego, L.F. Life cycle assessment of power-to-methane systems with CO_2 supplied by the chemical looping combustion of biomass. *Energy Convers. Manag.* **2022**, *267*, 115866. [CrossRef]
13. Ursúa, A.; Gandía, L.M.; Sanchis, P. Hydrogen Production From Water Electrolysis: Current Status and Future Trends. *Proc. IEEE* **2012**, *100*, 410–426. [CrossRef]
14. Blanco, H.; Nijs, W.; Ruf, J.; Faaij, A. Potential of Power-to-Methane in the EU energy transition to a low carbon system using cost optimization. *Appl. Energy* **2018**, *232*, 323–340. [CrossRef]
15. Götz, M.; Lefebvre, J.; Mörs, F.; McDaniel Koch, A.; Graf, F.; Bajohr, S.; Reimert, R.; Kolb, T. Renewable Power-to-Gas: A technological and economic review. *Renew. Energy* **2016**, *85*, 1371–1390. [CrossRef]
16. Gassner, M.; Maréchal, F. Thermo-economic optimisation of the integration of electrolysis in synthetic natural gas production from wood. *Energy* **2008**, *33*, 189–198. [CrossRef]
17. Hausberger, A.L.; Knight, C.B.; Atwood, K. Development of Methanation Catalysts for the Synthetic Natural Gas Processes. In *Methanation of Synthesis Gas. Advances in Chemistry Vol. 146*; Seglin, L., Ed.; American Chemical Society: Washington, DC, USA, 1975; pp. 47–70.
18. Mills, G.A.; Steffgen, F.W. Catalytic Methanation. *Catal. Rev.* **1973**, *8*, 159–210. [CrossRef]
19. Weatherbee, G.D.; Bartholomew, C.H. Hydrogenation of CO_2 on Group VIII Metals, I. Specific Activity of Ni/SiO$_2$. *J. Catal.* **1981**, *68*, 67–76. [CrossRef]
20. Wang, W.; Wang, S.; Ma, X.; Gong, J. Recent advances in catalytic hydrogenation of carbon dioxide. *Chem. Soc. Rev.* **2011**, *40*, 3703–3727. [CrossRef]
21. Aziz, M.A.A.; Jalil, A.A.; Triwahyono, S.; Ahmad, A. CO_2 methanation over heterogeneous catalysts: Recent progress and future prospects. *Green Chem.* **2015**, *17*, 2647. [CrossRef]
22. Su, X.; Xu, J.; Liang, B.; Duan, H.; Hou, B.; Huang, Y. Catalytic carbon dioxide hydrogenation to methane: A review of recent studies. *J. Energy Chem.* **2016**, *25*, 553–565. [CrossRef]
23. Younas, M.; Kong, L.L.; Bashir, M.J.K.; Nadeem, H.; Shehzad, A.; Sethupathi, S. Recent Advancements, Fundamental Challenges, and Opportunities in Catalytic Methanation of CO_2. *Energy Fuels* **2016**, *30*, 8815–8831. [CrossRef]

24. Frontera, P.; Macario, A.; Ferraro, M.; Antonucci, P.L. Supported Catalysts for CO_2 Methanation: A Review. *Catalysts* **2017**, *7*, 59. [CrossRef]

25. Ducamp, J.; Bengaouer, A.; Baurens, P.; Fechete, I.; Turek, P.; Garin, F. *Statu quo* sur la methanation du dioxide de carbone: Une revue de la littérature. *Comptes Rendus Chim.* **2018**, *21*, 427–469. [CrossRef]

26. Sreedhar, I.; Varun, Y.; Singh, S.A.; Venugopal, A.; Reddy, B.M. Developmental trends in CO_2 methanation using various catalysts. *Catal. Sci. Technol.* **2019**, *9*, 4478. [CrossRef]

27. Mebrahtu, C.; Krebs, F.; Abate, S.; Perathoner, S.; Centi, G.; Palkovits, R. CO_2 Methanation: Principles and Challenges. Stud. Surf. *Sci. Catal.* **2019**, *178*, 85–103.

28. Ashok, J.; Pati, S.; Hongmaronon, P.; Tianxi, Z.; Junmei, Z.; Kawi, S. A review of recent catalyst advances in CO_2 methanation processes. *Catal. Today* **2020**, *356*, 471–489. [CrossRef]

29. Le, W.J.; Li, C.; Prajitno, H.; Yoo, J.; Patel, J.; Yang, Y.; Lim, S. Recent trend in thermal catalytic low temperature CO_2 methanation: A critical review. *Catal. Today* **2021**, *368*, 2–19. [CrossRef]

30. Tsiotsias, A.I.; Charision, N.D.; Yentekakis, I.V.; Goula, M.A. Bimetallic Ni-Based Catalysts for CO_2 Methanation: A Review. *Nanomaterials* **2021**, *11*, 28. [CrossRef] [PubMed]

31. Wang, Z.; Wang, L.; Cui, Y.; Xing, Y.; Su, W. Research on nickel-based catalysts for carbon dioxide methanation combined with literature measurements. *J. CO^2 Util.* **2022**, *63*, 102117. [CrossRef]

32. Vance, C.K.; Bartholomew, C.H. Hydrogenation of carbon dioxide on group VIII metals. III, Effects of support on Activity/selectivity and adsorption properties of nickel. *Appl. Catal.* **1983**, *7*, 169–177. [CrossRef]

33. Abate, S.; Mebrahtu, C.; Giglio, E.; Deorsola, F.; Bensaid, S.; Perathoner, S.; Pirone, R.; Centi, G. Catalytic Performance of γ-$Al_2O_3-ZrO_2-TiO_2-CeO_2$ Composite Oxide Supported Ni-Based Catalysts for CO_2 Methanation. *Ind. Eng. Chem. Res.* **2016**, *55*, 4451–4460. [CrossRef]

34. Le, T.A.; Kim, M.S.; Lee, S.H.; Kim, T.W.; Park, E.D. CO and CO_2 methanation over supported Ni catalysts. *Catal. Today* **2017**, *293–294*, 89–96. [CrossRef]

35. Martínez, J.; Hernández, E.; Alfaro, S.; López Medina, R.; Valverde Aguilar, G.; Albiter, E.; Valenzuela, M.A. High Selectivity and Stability of Nickel Catalysts for CO_2 Methanation: Support Effects. *Catalysts* **2019**, *9*, 24. [CrossRef]

36. Gac, W.; Zawadzki, W.; Rotko, M.; Greluk, M.; Słowik, G.; Kolb, G. Effects of support composition on the performance of nickel catalysts in CO_2 methanation reaction. *Catal. Today* **2020**, *357*, 468–482. [CrossRef]

37. Shen, L.; Xu, J.; Zhu, M.; Han, Y.-F. Essential Role of the Support for Nickel-Based CO_2 Methanation Catalysts. *ACS Catal.* **2020**, *10*, 14581–14591. [CrossRef]

38. Aldana, P.A.U.; Ocampo, F.; Kobl, K.; Louis, B.; Thibault-Starzyk, F.; Daturi, M.; Bazin, P.; Thomas, S.; Roger, A.C. Catalytic CO_2 valorization into CH_4 on Ni-based ceria-zirconia. Reaction mechanism by operando IR spectroscopy. *Catal. Today* **2013**, *215*, 201–207. [CrossRef]

39. Pan, Q.; Peng, J.; Sun, T.; Wang, S.; Wang, S. Insight into the reaction route of CO_2 methanation: Promotion effect of medium basic sites. *Catal. Commun.* **2014**, *45*, 74–78. [CrossRef]

40. Muroyama, H.; Tsuda, Y.; Asakoshi, T.; Masitah, H.; Okanishi, T.; Matsui, T.; Eguchi, K. Carbon dioxide methanation over Ni catalysts supported on various metal oxides. *J. Catal.* **2016**, *343*, 178–184. [CrossRef]

41. Guo, X.; Traitangwong, A.; Hu, M.; Zuo, C.; Meeyoo, V.; Peng, Z.; Li, C. Carbon Dioxide Methanation over Nickel-Based Catalysts Supported on Various Mesoporous Material. *Energy Fuels* **2018**, *32*, 3681–3689. [CrossRef]

42. Liang, C.; Zhang, L.; Zheng, Y.; Zhang, S.; Liu, Q.; Gao, G.; Dong, D.; Wang, Y.; Xu, L.; Hu, X. Methanation of CO_2 over nickel catalysts: Impacts of acidic/basic sites on formation of the reaction intermediates. *Fuel* **2020**, *262*, 116521. [CrossRef]

43. Ilsemann, J.; Murshed, M.M.; Gesing, T.M.; Kopyscinski, J.; Bäumer, M. On the support dependency of the CO_2 methanation—Decoupling size and support effects. *Catal. Sci. Technol.* **2021**, *11*, 4098. [CrossRef]

44. Gao, X.; Wang, Z.; Huang, Q.; Jiang, M.; Askari, S.; Dewangan, N.; Kawi, S. State-of-art modifications of heterogeneous catalysts for CO_2 methanation—Active sites, surface basicity and oxygen defects. *Catal. Today* **2022**, *402*, 88–103. [CrossRef]

45. Kattel, S.; Liu, P.; Chen, J.G. Tuning Selectivity of CO_2 Hydrogenation Reactions at the Metal/Oxide Interface. *J. Am. Chem. Soc.* **2017**, *139*, 9739–9754. [CrossRef]

46. Cárdenas-Arenas, A.; Quindimil, A.; Davó-Quiñonero, A.; Bailón-García, E.; Lozano-Castelló, D.; De-La-Torre, U.; Pereda-Ayo, B.; González-Marcos, J.A.; González-Velasco, J.R.; Bueno-López, A. Isotopic and in situ DRIFTS study of the CO_2 methanation mechanism using Ni/CeO_2 and Ni/Al_2O_3 catalysts. *Appl. Catal. B Environ.* **2020**, *265*, 118538. [CrossRef]

47. Pu, T.; Shen, L.; Liu, X.; Cao, X.; Xu, J.; Wachs, I.E.; Zhu, M. Formation and influence of surface hydroxyls on product selectivity during CO_2 hydrogenation by Ni/SiO_2 catalysts. *J. Catal.* **2021**, *400*, 154–196. [CrossRef]

48. Lee, Y.H.; Ahn, J.Y.; Nguyen, D.D.; Chang, S.W.; Kim, S.S.; Lee, S.M. Role of oxide support in Ni based catalysts for CO_2 methanation. *RSC Adv.* **2021**, *11*, 17648. [CrossRef]

49. Solis-Garcia, A.; Zepeda, T.A.; Fierro-Gonzalez, J.C. Spectroscopic evidence of surface species during CO_2 methanation catalyzed by supported metals: A review. *Catal. Today* **2022**, *394–396*, 2–12. [CrossRef]

50. Meunier, F.C. Hydrogenation of CO and CO_2: Contributions of IR *operando* studies. *Catal. Today* **2022**, *in press*. [CrossRef]

51. Miao, B.; Ma, S.S.K.; Wang, X.; Su, H.; Chan, S.H. Catalysis mechanisms of CO_2 and CO methanation. *Catal. Sci. Technol.* **2016**, *6*, 4048. [CrossRef]

52. Lin, W.; Stocker, K.M.; Schatz, G.C. Mechanisms of Hydrogen-Assisted CO_2 Reduction on Nickel. *J. Am. Chem. Soc.* **2017**, *139*, 4663–4666. [CrossRef] [PubMed]

53. Ray, K.; Deo, G. A potential descriptor for the CO_2 hydrogenation to CH_4 over Al_2O_3 supported Ni and Ni-based alloy catalysts. *Appl. Catal. B Environ.* **2019**, *18*, 525–537. [CrossRef]

54. Vogt, C.; Groeneveld, E.; Kamsma, G.; Nachtegaal, M.; Lu, L.; Kiely, C.J.; Berben, P.H.; Meirer, F.; Weckhuysen, B.M. Unravelling structure sensitivity in CO_2 hydrogenation over nickel. *Nat. Catal.* **2018**, *1*, 127–134. [CrossRef]

55. Beierlein, D.; Häussermann, D.; Pfeifer, M.; Schwarz, T.; Stöwe, K.; Traa, Y.; Klemm, E. Is the CO_2 methanation on highly loaded Ni-Al_2O_3 catalysts really structure sensitive? *Appl. Catal. B Environ.* **2019**, *247*, 200–219. [CrossRef]

56. Lozano-Reis, P.; Prats, H.; Gamallo, P.; Illas, F.; Sayós, R. Multiscale Study of the Mechanism of Catalytic CO_2 Hydrogenation: Role of the Ni(111) Facets. *ACS. Catal.* **2020**, *10*, 8077–8089. [CrossRef]

57. Villagra-Soza, F.; Godoy, S.; Karelovic, A.; Jiménez, R. Scrutinizing the mechanism of CO_2 hydrogenation over Ni, Co and bimetallic NiCo surfaces: Isotopic measurements, operando-FTIR experiments and kinetics modelling. *J. Catal.* **2022**, *414*, 1–15. [CrossRef]

58. Bentaleb, F.; Marceau, E. Influence of the textural properties of porous aluminas on the reducibility of Ni/Al_2O_3 catalysts. *Microporous Mesoporous Mater.* **2012**, *146*, 40–44. [CrossRef]

59. Bartholomew, C.H.; Farrauto, R.J. Chemistry of nickel-alumina catalysts. *J. Catal.* **1976**, *45*, 41–53. [CrossRef]

60. Gandía, L.M.; Montes, M. Effect of the reduction temperature on the selectivity of the high temperature reaction of acetone and hydrogen over alumina and titania supported nickel and cobalt catalysts. *J. Mol. Catal.* **1994**, *94*, 347–367. [CrossRef]

61. Li, Y.; Zhang, B.; Tang, X.; Xu, Y.; Shen, W. Hydrogen production from methane decomposition over Ni/CeO_2 catalysts. *Catal. Commun.* **2006**, *7*, 380–386. [CrossRef]

62. Zheng, H.; Liao, W.; Ding, J.; Xu, F.; Jia, A.; Huang, W.; Zhang, Z. Unveiling the Key Factors in Determining Activity and Selectivity of CO_2 Hydrogenation over Ni/CeO_2 Catalysts. *ACS Catal.* **2022**, *12*, 15451–15462. [CrossRef]

63. Hao, Z.; Shen, J.; Lin, S.; Han, X.; Chang, X.; Liu, J.; Li, M.; Ma, X. Decoupling the effect of Ni particle size and surface oxygen deficiencies in CO_2 methanation over ceria supported Ni. *Appl. Catal. B Environ.* **2021**, *286*, 119922. [CrossRef]

64. Xie, Y.; Chen, J.; Wu, X.; Wen, J.; Zhao, R.; Li, Z.; Tian, G.; Zhang, Q.; Ning, P.; Hao, J. Frustrated Lewis Pairs Boosting Low-Temperature CO_2 Methanation Performance over Ni/CeO_2 Nanocatalysts. *ACS Catal.* **2022**, *12*, 10587–10602. [CrossRef]

65. Ye, R.-P.; Li, Q.; Gong, W.; Wang, T.; Razink, J.J.; Lin, L.; Qin, Y.-Y.; Zhou, Z.; Adidharma, H.; Tange, J.; et al. High-performance of nanostructured Ni/CeO_2 catalyst on CO_2 methanation. *Appl. Catal. B Environ.* **2020**, *268*, 118474. [CrossRef]

66. Italiano, C.; Llorca, J.; Pino, L.; Ferraro, M.; Antonucci, V.; Vita, A. CO and CO_2 methanation over Ni catalysts supported on CeO_2, Al_2O_3 and Y_2O_3 oxides. *Appl. Catal. B Environ.* **2020**, *264*, 118494. [CrossRef]

67. Trovarelli, A. Catalytic Properties of Ceria and CeO_2-Containing Materials. *Catal. Rev.-Sci. Eng.* **1996**, *38*, 439–520. [CrossRef]

68. Ocampo, F.; Louis, B.; Roger, A.-C. Methanation of carbon dioxide over nickel-based $Ce_{0.72}Zr_{0.28}O_2$ mixed oxide catalysts prepared by sol–gel method. *Appl. Catal. A Gen.* **2009**, *369*, 90–96. [CrossRef]

69. Vrijburg, W.L.; van Helden, J.W.A.; Parastaev, A.; Groeneveld, E.; Pidko, E.A.; Hensen, E.J.M. Ceria–zirconia encapsulated Ni nanoparticles for CO_2 methanation. *Catal. Sci. Technol.* **2019**, *9*, 5001. [CrossRef]

70. Unwiset, P.; Chanapattharapol, K.C.; Kidkhunthod, P.; Poo-arporn, Y.; Ohtani, B. Catalytic activities of titania-supported nickel for carbon-dioxide methanation. *Chem. Eng. Sci.* **2020**, *228*, 115955. [CrossRef]

71. van de Loosdrecht, J.; van der Kraan, A.M.; van Dillen, A.J.; Geus, J.W. Metal–Support Interaction: Titania-Supported and Silica-Supported Nickel Catalysts. *J. Catal.* **1997**, *170*, 217–226. [CrossRef]

72. Ho, S.-W.; Chu, C.-Y.; Chen, S.-G. Effect of Thermal Treatment on the Nickel State and CO Hydrogenation Activity of Titania-Supported Nickel Catalysts. *J. Catal.* **1998**, *178*, 34–48. [CrossRef]

73. Wang, W.; Wang, S.; Ma, X.; Gong, J. Crystal structures, acid–base properties, and reactivities of $Ce_xZr_{1-x}O_2$ catalysts. *Catal. Today* **2009**, *148*, 323–328. [CrossRef]

74. Mao, Z.; Campbell, C.T. Apparent Activation Energies in Complex Reaction Mechanisms: A Simple Relationship via Degrees of Rate Control. *ACS Catal.* **2019**, *9*, 9465–9473. [CrossRef]

75. Slot, T.K.; Riley, N.; Shiju, N.R.; Medlin, J.W.; Rothenberg, G. An experimental approach for controlling confinement effects at catalyst interfaces. *Chem. Sci.* **2020**, *11*, 11024. [CrossRef]

76. Vannice, M.A. *Kinetics of Catalytic Reactions*; Springer: New York, NY, USA, 2010; p. 145.

77. Schmider, D.; Maier, L.; Deutschmann, O. Reaction Kinetics of CO and CO_2 Methanation over Nickel. *Ind. Eng. Chem. Res.* **2021**, *60*, 5792–5805. [CrossRef]

78. Garbarino, G.; Bellotti, D.; Finocchio, E.; Magistri, L.; Busca, G. Methanation of carbon dioxide on Ru/Al_2O_3: Catalytic activity and infrared study. *Catal. Today* **2016**, *277*, 21–28. [CrossRef]

79. Zhang, Z.; Verykios, X.E.; MacDonald, S.M.; Affrossman, S. Comparative Study of Carbon Dioxide Reforming of Methane to Synthesis Gas over Ni/La_2O_3 and Conventional Nickel-Based Catalysts. *J. Phys. Chem.* **1996**, *100*, 744–754. [CrossRef]

80. Montanari, T.; Castoldi, L.; Lietti, L.; Busca, G. Basic catalysis and catalysis assisted by basicity: FT-IR and TPD characterization of potassium-doped alumina. *Appl. Catal. A Gen.* **2011**, *400*, 61–69. [CrossRef]

81. Davydov, A. *Molecular Spectroscopy of Oxide Catalyst Surfaces*; Sheppard, N.T., Ed.; John Wiley & Sons, Ltd.: Chichester, UK, 2003.

82. Bechoux, K.; Marie, O.; Daturi, M.; Delahay, G.; Petitto, C.; Rousseau, S.; Blanchard, G. Infrared evidence of room temperature dissociative adsorption of carbon monoxide over Ag/Al_2O_3. *Catal. Today* **2012**, *197*, 155–161. [CrossRef]

83. Busca, G.; Lorenzelli, V. Infrared spectroscopic identification of species arising from reactive adsorption of carbon oxides on metal oxide surfaces. *Mater. Chem.* **1982**, *7*, 89–126. [CrossRef]

84. Busca, G.; Lamotte, J.; Lavalley, J.; Lorenzelli, V. FT-IR Study of the Adsorption and Transformation of Formaldehyde on Oxide Surfaces. *J. Am. Chem. Soc.* **1987**, *109*, 5197–5202. [CrossRef]

85. Gao, J.; Wang, Y.; Ping, Y.; Hu, D.; Xu, G.; Gu, F.; Su, F. A thermodynamic analysis of methanation reactions of carbon oxides for the production of synthetic natural gas. *RSC Adv.* **2012**, *2*, 2358–2368. [CrossRef]

86. Bian, Z.; Chan, Y.M.; Yu, Y.; Kawi, S. Morphology dependence of catalytic properties of Ni/CeO$_2$ for CO$_2$ methanation: A kinetic and mechanism study. *Catal. Today* **2020**, *347*, 31–38. [CrossRef]

87. Finocchio, E.; Daturi, M.; Binet, C.; Lavalley, J.C.; Blanchard, G. Thermal evolution of the adsorbed methoxy species on Ce$_x$Zr$_{1-x}$O$_2$ solid solution samples: A FT-IR study. *Catal. Today* **1999**, *52*, 53–63. [CrossRef]

88. Konishcheva, M.V.; Potemkin, D.I.; Badmaev, S.D.; Snytnikov, P.V.; Paukshtis, E.; Sobyanin, V.; Parmon, V.N. On the Mechanism of CO and CO$_2$ Methanation Over Ni/CeO$_2$ Catalysts. *Top. Catal.* **2016**, *59*, 1424–1430. [CrossRef]

89. Lustemberg, P.G.; Bosco, M.V.; Bonivardi, A.; Busnengo, H.F.; Ganduglia-pirovano, M.V. Insights into the Nature of Formate Species in the Decomposition and Reaction of Methanol over Cerium Oxide Surfaces: A Combined Infrared Spectroscopy and Density Functional Theory Study. *J. Phys. Chem. C* **2015**, *119*, 21452–21464. [CrossRef]

90. Bazin, P.; Thomas, S.; Marie, O.; Daturi, M. New insights into the methanol oxidation mechanism over Au/CeO$_2$ catalyst through complementary kinetic and FTIR operando SSITKA approaches. *Catal. Today* **2012**, *182*, 3–11. [CrossRef]

91. Daturi, M.; Binet, C.; Lavalley, J.C.; Galtayries, A.; Sporken, R. Surface investigation on Ce$_{(x)}$Zr$_{(1-x)}$O$_2$ compounds. *Phys. Chem. Chem. Phys.* **1999**, *1*, 5717–5724. [CrossRef]

92. Binet, C.; Daturi, M.; Lavalley, J.-C. IR study of polycrystalline ceria properties in oxidised and reduced states. *Catal. Today* **1999**, *50*, 207–225. [CrossRef]

93. Rousseau, S.; Marie, O.; Bazin, P.; Daturi, M.; Verdier, S.; Harlé, V. Investigation of Methanol Oxidation over Au/Catalysts Using Operando IR Spectroscopy: Determination of the Active Sites, Intermediate/Spectator Species, and Reaction Mechanism. *J. Am. Chem. Soc.* **2010**, *132*, 10832–10841. [CrossRef]

94. Riguetto, B.A.; Damyanova, S.; Gouliev, G.; Marques, C.M.P.; Petrov, L.; Bueno, J.M.C. Surface Behavior of Alumina-Supported Pt Catalysts Modified with Cerium as Revealed by X-ray Diffraction, X-ray Photoelectron Spectroscopy, and Fourier Transform Infrared Spectroscopy of CO Adsorption. *J. Phys. Chem. B* **2004**, *108*, 5349–5358. [CrossRef]

95. Daturi, M.; Binet, C.; Lavalley, J.C.; Blanchard, G. Surface FTIR investigations on Ce$_x$Zr$_{1-x}$O$_2$ system. *Surf. Interface Anal.* **2000**, *30*, 273–277. [CrossRef]

96. Fukuhara, C.; Hayakawa, K.; Suzuki, Y.; Kawasaki, W.; Watanabe, R. A novel nickel-based structured catalyst for CO$_2$ methanation: A honeycomb-type Ni/CeO$_2$ catalyst to transform greenhouse gas into useful resources. *Appl. Catal. A Gen.* **2017**, *532*, 12–18. [CrossRef]

97. Guo, Y.; Mei, S.; Yuan, K.; Wang, D.-J.; Liu, H.-C.; Yan, C.-H.; Zhang, Y.-W. Low-Temperature CO$_2$ Methanation over CeO$_2$-Supported Ru Single Atoms, Nanoclusters, and Nanoparticles Competitively Tuned by Strong Metal−Support Interactions and H-Spillover Effect. *ACS Catal.* **2018**, *8*, 6203–6215. [CrossRef]

98. Solis-Garcia, A.; Louvier-Hernandez, J.F.; Almendarez-Camarillo, A.; Fierro-Gonzalez, J.C. Participation of surface bicarbonate, formate and methoxy species in the carbon dioxide methanation catalyzed by ZrO$_2$-supported Ni. *Appl. Catal. B Environ.* **2017**, *218*, 611–620. [CrossRef]

99. Ashok, J.; Ang, M.L.; Kawi, S. Enhanced activity of CO$_2$ methanation over Ni/CeO$_2$-ZrO$_2$ catalysts: Influence of preparation methods. *Catal. Today* **2017**, *281*, 304–311. [CrossRef]

100. Daturi, M.; Finocchio, E.; Binet, C.; Lavalley, J.; Fally, F.; Perrichon, V.; Vidal, H.; Hickey, N.; Kaspar, J. Reduction of High Surface Area CeO$_2$-ZrO$_2$ Mixed Oxides. *J. Phys. Chem. B* **2000**, *104*, 9186–9194. [CrossRef]

101. Kähler, K.; Holz, M.C.; Rohe, M.; Van Veen, A.C.; Muhler, M. Methanol oxidation as probe reaction for active sites in Au/ZnO and Au/TiO$_2$ catalysts. *J. Catal.* **2013**, *299*, 162–170. [CrossRef]

102. Wu, W.; Chuang, C.; Lin, J. Bonding Geometry and Reactivity of Methoxy and Ethoxy Groups Adsorbed on Powdered TiO$_2$. *J. Phys. Chem. B* **2000**, *104*, 8719–8724. [CrossRef]

103. Manzoli, M.; Chiorino, A.; Boccuzzi, F. Decomposition and combined reforming of methanol to hydrogen: A FTIR and QMS study on Cu and Au catalysts supported on ZnO and TiO$_2$. *Appl. Catal. B Environ.* **2005**, *57*, 201–209. [CrossRef]

104. Chen, T.; Feng, Z.; Wu, G.; Shi, J.; Ma, G.; Ying, P.; Li, C. Mechanistic Studies of Photocatalytic Reaction of Methanol for Hydrogen Production on Pt/TiO$_2$ by in situ Fourier Transform IR and Time-Resolved IR Spectroscopy. *J. Phys. Chem. B* **2007**, *111*, 8005–8014. [CrossRef]

105. Chuang, C.-C.; Chen, C.-C.; Lin, J.-L. Photochemistry of Methanol and Methoxy Groups Adsorbed on Powdered TiO$_2$. *J. Phys. Chem. B* **1999**, *103*, 2439–2444. [CrossRef]

106. Wang, Z.; Qi, J.; Yang, N.; Yu, R.; Wang, D. Core-shell nano/microstructures for heterogeneous tandem catalysis. *Mater. Chem. Front.* **2021**, *5*, 1126. [CrossRef]

107. González-Castaño, M.; González-Arias, J.; Bobadilla, L.F.; Ruíz-López, E.; Odriozola, J.A.; Arellano-García, H. In-Situ Drifts Steady-State Study of CO$_2$ and Co Methanation Over Ni-Promoted Catalysts. *Fuel* **2023**, *338*, 127241. [CrossRef]

108. Gil, A.; Díaz, A.; Gandía, L.M.; Montes, M. Influence of the preparation method and the nature of the support on the stability of nickel catalysts. *Appl. Catal. A Gen.* **1994**, *109*, 167–179. [CrossRef]

109. Gandía, L.M.; Diaz, A.; Montes, M. Selectivity in the High-Temperature Hydrogenation of Acetone with Silica-Supported Nickel and Cobalt catalysts. *J. Catal.* **1995**, *157*, 461–471. [CrossRef]
110. Wuttke, S.; Bazin, P.; Vimont, A.; Serre, C.; Seo, Y.-K.; Hwang, Y.K.; Chang, J.-S.; Férey, G.; Daturi, M. Discovering the Active Sites for C3 Separation in MIL-100(Fe) by Using Operando IR Spectroscopy. *Chem. Eur. J.* **2012**, *18*, 11959–11967. [CrossRef] [PubMed]
111. Thomas, S.; Marie, O.; Bazin, P.; Lietti, L.; Visconti, C.G.; Corbetta, M.; Manenti, F.; Daturi, M. Modelling a reactor cell for operando IR studies: From qualitative to fully quantitative kinetic investigations. *Catal. Today* **2017**, *283*, 176–184. [CrossRef]